

2. EXPLANATORY NOTES¹

Shipboard Scientific Party²

INTRODUCTION

The “Explanatory Notes” chapter presents information that will help the reader understand our shipboard observations and measurements, which are the basis for the preliminary conclusions found throughout this volume, and also help the interested investigator select samples for further analysis. This information concerns only shipboard operations and analyses reported in the Leg 208 *Initial Reports* volume of the *Proceedings of the Ocean Drilling Program* (ODP). Methods used by various investigators for shore-based analyses of Leg 208 samples will be described in the individual scientific contributions published in the *Scientific Results* volume and in publications in various professional journals.

A significant part of this chapter is material that has been presented in previous ODP *Proceedings* volumes, as ODP strives to keep well-established and accepted standard procedures consistent from leg to leg. Other issues more specific to Leg 208, such as instruments, methods, and procedures that were relatively new in the framework of the evolving ODP shipboard environment or that were used specifically to address Leg 208 objectives, are presented here in greater detail.

OPERATIONS

Site Locations

At all Leg 208 sites, Global Positioning System (GPS) coordinates from precruise site surveys were used to position the vessel on site. Once the vessel was positioned on a site, the thrusters were lowered and a reference beacon was deployed. Although the automated stationkeeping system of the vessel usually uses GPS data, the beacon provides a backup reference in case of problems with the transmission of satellite

¹Examples of how to reference the whole or part of this volume.

²Shipboard Scientific Party addresses.

data. The final site position was the mean position calculated from the GPS data collected over a significant portion of the time the site was occupied. At the end of operations at a site, the beacon was retrieved and the thrusters were retracted before the vessel proceeded to the next site.

Drilling Operations

Two coring systems were used during Leg 208: the advanced hydraulic piston corer (APC) and the extended core barrel (XCB). The APC is a “cookie cutter”-type system that cuts cores with minimal coring disturbance. The drill pipe is pressured up until one or two shear pins that hold the inner barrel to the outer barrel fail. The inner barrel strikes out and cuts the core. The driller can detect a successful cut or “full stroke” by the pressure gauge on the rig floor. Whenever possible, the APC was used during Leg 208 because it yields the least disturbed cores.

When “APC refusal” occurs in a hole before the target depth is reached, the XCB is used to advance the hole. The XCB is a rotary system with a small cutting shoe extending below the large rotary bit. The smaller bit can cut a semi-indurated core with less torque and fluid circulation than the main bit and thus optimizes recovery. If the formation becomes even more indurated, the rotary core barrel (RCB) is used. The RCB system is the most conventional drilling system, but it was not needed during Leg 208.

Both the APC and XCB systems use the same bottom-hole assembly (BHA), and switching from one to the other does not require a pipe trip. The standard BHA used at all Leg 208 sites comprised a 9⁷/₈-in APC/XCB polycrystalline diamond bit, a bit sub, a seal bore drill collar, a landing saver sub, a modified top sub, a modified head sub, a nonmagnetic drill collar, five 8¹/₄-in drill collars, a tapered drill collar, six joints of 5¹/₂-in drill pipe, and one crossover sub. The BHA length was 136 m with a total weight of 35,000 lb. When it became necessary to drill over stuck core barrels, the standard steel barrel assembly was used instead of the nonmagnetic barrel. A lockable float valve was used instead of the standard float assembly if the possibility of logging existed.

APC refusal is conventionally defined in two ways: (1) the piston fails to achieve a complete stroke (as determined from the pump pressure reading) because the formation is too hard, and (2) excess force (>60,000 lb) is required to pull the core barrel out of the formation because of friction. In the case where a full stroke could not be achieved, one or two more attempts were typically made with the APC and each time the bit was advanced by the length of recovered core. After three consecutive strikes with incomplete recovery, the APC was pulled out and the hole was advanced with the XCB. In the cases where full stroke could be achieved but excessive force could not retrieve the barrel, the core barrel was “drilled over” (i.e., after the inner core barrel was successfully shot into the formation, the rotary bit was advanced to total depth to free the APC barrel). This strategy allowed a hole to be advanced much farther with the APC, the preferred drilling tool.

Each cored interval was ~9.5 m long, which is the length of a core barrel. In some cases, the drill string was drilled or “washed” ahead without recovering sediments to advance the drill bit to a target depth where core recovery needed to be resumed. Such advances were necessary where there were multiple holes at a site to ensure that coring gaps in one hole were covered by cored intervals in adjacent holes. Adjustments were also necessary to ensure that critical intervals of a few decimeters in length (Paleocene/Eocene [P/E] and Cretaceous/Paleogene

[K/P] boundary intervals) were recovered in the middle of a core rather than near the bottom or end.

Drilled and cored intervals are referred to in meters below rig floor (mbrf), which are measured from the dual elevator stool (DES) on the rig floor to the bottom of the drill pipe. Where sediments of substantial thickness cover the seafloor (as at all sites during Leg 208), the mbrf depth of the seafloor is determined with a mudline core, assuming 100% recovery for the cored interval in the first core. If the first core recovered a full barrel of sediment (missing the mudline), the seafloor reference depth of a previous or later hole was used. Water depth is calculated by subtracting the distance between the DES and sea level (typically 10–11 m, depending on the ship's load at a given time) from the mbrf depth. The water depth determined in this way (drill string measurement) usually differs from the precision depth recorder measurements by a few to several meters. The meters below seafloor (mbsf) depths of core tops are calculated by subtracting the seafloor depth in mbrf from the core-top depth in mbrf. The core-top datums from the driller are the ultimate depth reference for any further depth calculation procedures.

Core Handling and Analysis

As soon as cores arrived on deck, gas void samples and headspace samples were taken by means of a syringe, if applicable, for immediate analysis as part of the shipboard safety and pollution prevention program. Core catcher samples were taken for biostratigraphic analysis. When the core was cut in sections, whole-round samples were taken for shipboard interstitial water examinations. In addition, headspace gas samples were immediately taken from the ends of cut sections and sealed in glass vials for light hydrocarbon analysis.

Before splitting, whole-round core sections were run through the multisensor track (MST) and thermal conductivity measurements were taken. The cores were then split into working and archive halves, from bottom to top, so investigators should be aware that older material could have been transported upward on the split face of each section. The working half of each core was sampled for both shipboard analyses, such as physical properties, carbonate, and X-ray diffraction mineralogy, and shore-based studies. Shipboard sampling was kept at a minimum during Leg 208 to allow completion of a detailed sampling plan after the composite depth scale and sampling splice were built (see [“Composite Depth,”](#) p. 4). The archive halves were photographed with both black-and-white and color film, scanned with the digital imaging system (DIS), described visually and by means of smear slides, measured for color reflectance on the archive-half multisensor track (AMST), and run through the cryogenic magnetometer. Close-up photographs were taken of particular features for illustrations in site summary reports, as requested by scientists.

Both halves of the core were then put into labeled plastic tubes, sealed, and transferred to cold storage space aboard the ship. At the end of the leg, the cores were transferred from the ship into refrigerated trucks and to cold storage at the Bremen Core Repository of the Ocean Drilling Program in Bremen, Germany.

Curatorial Procedures and Sample Depth Calculations

Numbering of sites, holes, cores, and samples follows the standard ODP procedure. A full curatorial identifier for a sample consists of the following information: leg, site, hole, core number, core type, section number, and interval in centimeters measured from the top of the core section. For example, a sample identification of “208-1262A-1H-1, 10–12 cm” would represent a sample removed from the interval between 10 and 12 cm below the top of Section 1, Core 1 (H designates that this core was taken with the APC system) of Hole 1262A during Leg 208.

Cored intervals are also referred to in “curatorial” mbsf. The mbsf depth of a sample is calculated by adding the depth of the sample below the section top and the lengths of all higher sections in the core to the core-top datum measured with the drill string. A soft to semisoft sediment core from less than a few hundred mbsf expands upon recovery (typically 10%–20%), and the recovered interval does not match the cored interval. In addition, a coring gap typically occurs between cores, as shown by composite depth construction (see “[Composite Depth](#),” below) (i.e., some cored interval was lost during recovery or was never cut). Thus, a discrepancy exists between the drilling mbsf and the curatorial mbsf. For instance, the curatorial mbsf of a sample taken from the bottom of a core is larger than that of a sample from the top of the subsequent core, where the latter does correspond to the drilled core-top datum.

During Leg 208, multiple APC holes (two to four) were drilled at a site to construct a continuous composite section. This resulted in a meters composite depth (mcd) scale for each site that accommodates core expansion and drilling gaps through interhole correlation of closely spaced measurements of core physical properties (see “[Composite Depth](#),” below).

COMPOSITE DEPTH

The recovery of complete sediment sections of APC- and XCB-cored intervals was crucial to the paleoceanographic objectives of Leg 208. Drilling of parallel holes at Sites 1262 through 1267 was planned to ensure that intervals missing from one APC/XCB hole as a result of recovery gaps between cores could be recovered in an adjacent hole. Composite depth sections have been developed for all multiply cored sites to confirm their continuity of recovery.

Adjustments to the shipboard mbsf depth scale are required for several reasons (e.g., Ruddiman et al., 1987; Hagelberg et al., 1992). Elastic rebound and gas expansion of the sediment following core recovery causes the cored sediment sequence to be expanded relative to the cored interval. As a result, the composite depth scale grows downhole relative to the mbsf scale, typically on the order of 10%–20%. In addition, the ship’s motion, which is due to tides and heave, can affect the in situ depth at which a core is cut. Portions of the sediment sequence are usually missing, even between cores that have >100% nominal recovery.

A composite depth scale places coeval, laterally continuous stratigraphic features into a common frame of reference by shifting the mbsf depth scales of individual cores to maximize the correlation between holes. The individual cores are shifted vertically without permitting expansion or contraction of the relative depth scale within any core. A

horizontal feature present in recovered material from several holes will have, in the absence of local stratigraphic variations, approximately the same mcd but will most likely have different mbsf depths. Horizontal features will have exactly the same mcd in two holes at the correlation tie points. Most other intervals will not be precisely correlated (offsets of a few millimeters to several centimeters) because of differential stretching and squeezing within cores. APC recovery gaps between cores in one hole typically range from 0.5 to 2 m and rarely exceed 5 m. After establishing an mcd scale, complete stratigraphic records are spliced from the data of multiple holes.

The methods used during Leg 208 to construct composite depth and spliced sections were similar to those used during Leg 138 (Hagelberg et al., 1992) and subsequent paleoceanographic ODP legs (e.g., Legs 154, 160, 161, 162, 167, 171B, 172, 175, 177, 178, 181, 182, 184, 189, 198, 199, 202, and 207). For each site, the hole-to-hole correlation was based on 2.5- or 5-cm spaced hole core measurements of magnetic susceptibility (MS), gamma ray attenuation (GRA) bulk density, compressional wave (*P*-wave) velocity measured on the *P*-wave logger (PWL), and natural gamma radiation (NGR) measured on the whole-core MST as well as spectral reflectance and point-sensor MS measurements on split cores (see “**Physical Properties**,” p. 11). A new application, Splicer-integrator, was used to retrieve the MST and color reflectance data from the ODP online database (Janus) and to upload the affine and splicer tables into the database. The mcd scale was constructed using the program Splicer (version 2.2), available on the World Wide Web from the Lamont-Doherty Earth Observatory Borehole Research Group (LDEO-BRG) (www.ldeo.columbia.edu/BRG/ODP). Splicer allows various data sets from several holes at a given site to be correlated simultaneously.

Correlations were done visually by selecting a tie point from primarily the MS data and/or color reflectance data in one hole and comparing it directly with data from another hole. Features were aligned by adjusting the coring depths in mbsf, measured from the length of the drill string advance, on a core-by-core basis. No stretching, squeezing, or any other depth adjustments were made within an individual core. The core that had the most pristine record of the upper portion of the upper few meters of the sedimentary record, particularly the mudline, was chosen as the first (anchor) core of the composite section. The mcd of the first core was thus the same as its mbsf depth. A tie point that gave the preferred correlation was selected between data from this core and a core in an adjacent hole. All data from the second hole below the correlation point were vertically shifted to align the tie points horizontally between the holes. Once the depth adjustment was made, the shifted section became the reference section and a tie was made to a core from another hole. The process continued downhole, vertically shifting the data from one core at a time relative to data from the other hole. The tie points were added to the “affine” table, which records all of the depth adjustments that define the composite depth scale in mcd. The composite depth scale for each site is presented in tabular form in the “Composite Depth” section of each site chapter. For each core, the depth adjustment required to convert from the mbsf depth scale to the mcd scale is given as the cumulative depth offset added to the ODP curatorial sub-bottom depth (in mbsf).

For some intervals of some sites, and in the case of Site 1266 for almost the complete succession, several factors limited the success of building a complete composite section. In these cases, we applied a con-

stant growth rate, based on the average growth rate of either overlying or underlying spliced intervals or, in the case of Site 1266, the average growth rate of previous Leg 208 sites was used to construct a (partially) spliced composite depth section.

During the composite section construction procedure, a spliced record was assembled that provides a single representative sedimentary record suited for postcruise sampling and studies. Splice ties were established as close to the composite depth tie points as the Splicer program allowed. Intervals were chosen for the splice so that section continuity was maintained and disturbed intervals were avoided. Tables that give the splice tie points for the construction of the spliced records are presented in each site chapter. By definition, splice tie points always connect features with exactly the same composite depths. Other intervals may not correlate perfectly between adjacent holes because the cores are stretched and squeezed differentially during the coring process. Further adjustments to the composite depth section by detailed correlation that includes expanding and compressing the depth scale within individual core intervals are required to align all features exactly.

LITHOSTRATIGRAPHY

For each site chapter, lithostratigraphy and physical properties are presented within a single section titled “Lithostratigraphy.” The purpose of integrating these results is twofold: sediment composition strongly affects physical properties, and physical properties commonly provide distinct step changes that are used to define lithostratigraphic unit boundaries. Thus, combining these results for each site chapter integrates complementary data and reduces descriptive redundancy. Within the “Explanatory Notes” chapter, however, we address lithostratigraphy and physical properties separately, given their different analytical techniques, methodologies, and classifications.

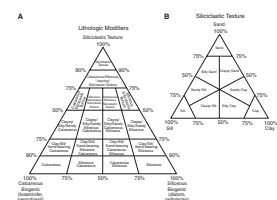
Sediment Classification

The lithologic classification scheme is based on three end-member grain components (i.e., siliceous biogenic, calcareous biogenic, and siliciclastic), the grain size of the siliciclastic component (i.e., clay, silt, or sand), and the degree of sediment induration (e.g., ooze vs. chalk, clay vs. claystone, etc.). Percentages of end-member grain components as well as siliciclastic textures were determined by smear slide examination and used to define lithologies reported on the visual core descriptions (VCDs) and barrel sheets. Area-based smear slide estimates of carbonate content often differed somewhat from mass-based coulometry determinations of carbonate content. Whereas these differences produced different sediment classifications, the smear slide–based classification was preferred. Each of the three end-member grain components is discussed below and is graphically related in Figure F1.

Calcareous Biogenic

Calcareous biogenic lithologies are composed of >50% biogenic grains, of which >50% are calcareous (Fig. F1A). Principal names indicate the degree of lithification and consist of ooze (i.e., readily deformed under the pressure of a finger or spatula blade), chalk (i.e., easily scratched by fingernail or edge of a spatula and cut by band or diamond

F1. Sediment classification, p. 42.



saw), and limestone (i.e., not scratched by fingernail or edge of a spatula and cut by band or diamond saw). Major modifiers (>25% of total composition) describe the nature of the calcareous biogenic (e.g., foraminifer and nannofossil), siliceous biogenic (e.g., diatom and radiolarian), or siliciclastic (e.g., sand, silt, and clay) grains. Minor modifiers (10%–25% of total composition) are described in similar terms, followed by the suffix “-bearing.” For example, a firm sediment composed of 5% foraminifers, 15% siliciclastic silt, 18% diatoms, and 60% nannofossils would be termed a silt- and diatom-bearing nannofossil chalk. Note that multiple modifiers are listed by increasing predominance and are followed by the principal name.

Siliceous Biogenic

Siliceous biogenic sediments are composed of >50% biogenic grains, of which >50% are siliceous (Fig. F1A). Principal names indicate the degree of lithification and consist of ooze (i.e., readily deformed under the pressure of a finger or spatula blade), porcellanite (i.e., easily scratched by fingernail or edge of a spatula and cut by band or diamond saw), and chert (i.e., not scratched by fingernail or edge of a spatula and cut by band or diamond saw). Major and minor modifiers are applied as above. For example, a soft sediment composed of 8% siliciclastic clay, 20% nannofossils, 35% radiolarians, and 37% diatoms would be termed a nannofossil-bearing radiolarian diatom ooze.

Siliciclastic

Siliciclastic sediments are composed of >50% siliciclastic grains and are classified according to the grain-size textures as clay (<3.9 μm), silt (3.9–63 μm), and sand (>63 μm –2.0 mm). The percentages of these grain-size textures define the principal siliciclastic names as outlined in Figure F1B. If the sediment is indurated (i.e., not easily scratched by fingernail or spatula edge), the suffix “-stone” is added (e.g., claystone, siltstone, and sandstone). In addition, the terms “conglomerate” and “breccia” are principal names for gravels with well-rounded and angular clasts, respectively. Major and minor modifiers for siliciclastic (e.g., quartz, feldspar, glauconite, mica, and lithic) and biogenic components are applied as above. For example, a sediment composed of 15% foraminifers, 25% glauconite, and 60% sand would be termed a foraminifer-bearing glauconitic sand. A sediment composed of 65% gravel and 35% silt would be termed a silty gravel. A sediment composed of 20% volcanic ash, 30% silt, and 50% sand would be termed an ash-bearing silty sand.

Sediment Description

Whole-core sections were analyzed by MST and measured for thermal conductivity (see “**Physical Properties**,” p. 11). All APC and most XCB core sections were split from bottom to top by pulling a double-hook razor and wire assembly lengthwise through their center. This process frequently disrupted core surfaces into an irregular series of roughly parallel tears that obscured sedimentary features and core disturbance and also biased digital and photographic imaging toward darker coloration and overall lower sediment lightness (L^*). Initially, tears in the archive half were not altered or were partially flattened perpendicular to the core axis with a clean stainless steel or glass-slide

edge. Subsequent experimentation produced the more effective method of covering each core section with Glad Wrap clear plastic then annealing the tears with gentle stroking with a spatula toward the core bottom at a slight angle to the center axis of the core surface. This process revealed fine-scale (millimeter scale) features that were otherwise obscured (Fig. F2). More indurated XCB core sections were split from bottom to top by supersaw followed by rinsing the surface of both the archive and working halves with water. Thin intervals of limestone, siliceous limestone, and chert were split by diamond rocksaw.

Digital Imaging

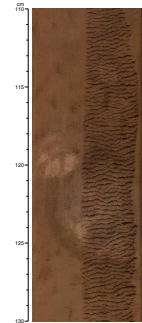
All archive halves were scanned using the Geotek DIS. The DIS uses an interference filter and three line-scan charge-coupled device arrays (1024 pixels each) to continuously record the three red-green-blue (RGB) color channels at an 8-bit dynamic range. The standard DIS configuration produces 300 dpi on an 8-cm-wide core with a zoom capability of up to 1200 dpi on a 2-cm-wide core. Synchronization and track control is better than 0.02 mm, and a framestore card contains 48 MB of RAM for image acquisition. The camera aperture was set to maximize contrast within the lightest-colored sediment of each core. Each archive half, along with a neutral gray color chip and section identification bar code label, was DIS scanned to produce a TIFF (no compression) and a SID (compression) image. Using the Geotek Image Tools utilities, the SID files were resampled to produce a JPEG file with a resolution of ~300 dpi. The JPEG files are viewable using the Web browser as “photo table” composite images. Profiles for each RGB channel were produced by averaging pixels in 3 cm × 0.5 cm rectangles along the core’s central axis. The DIS system was calibrated for black and white approximately every 12 hr, although no notable calibration drift occurred during Leg 208. During scanning of Site 1262 cores, we discovered that the software processing did not completely correct for images scanned at different aperture settings to a common brightness level. Therefore, subsequent Sites 1263 through 1267 were scanned at a fixed aperture setting of 11.

Diffuse Color Reflectance Spectrophotometry

Archive halves were measured at 2.5-cm intervals using a Minolta Spectrophotometer (model CM-2002) mounted on the AMST. For “critical intervals” such as the P/E and K/P boundaries, archive halves were scanned at 1-cm intervals. Prior to measurement, each core section’s surface was covered with Glad Wrap clear plastic to maintain a clean spectrometer window. Spectrophotometric analysis produced three types of data: (1) intensity values for 31 contiguous 10-nm-wide bands across the 400- to 700-nm interval of the visible light spectrum; (2) L^* , a^* , and b^* values, where L^* (lightness) is a total reflectance index ranging from 0% to 100%, a^* is the green (–) to red (+) chromaticity, and b^* is the blue (–) to yellow (+) chromaticity; and (3) Munsell color values. Spectrophotometer calibration was performed every 24 hr with no notable change through time. Additional information about the measurement and interpretation of spectral data with the Minolta spectrophotometer is presented in Balsam et al. (1997, 1998, 1999).

We caution end users of these spectrophotometric data regarding three issues. First, data precision should not be confused with data accuracy; core disturbances, particularly biscuiting and flow-in, introduce

F2. Smoothing example, p. 43.



spurious information. Furthermore, many cores from Site 1262 were not smoothed (Fig. F2), which slightly biases the digital and spectrophotometric data toward darker values. We recommend careful consideration of appropriate core photos and disturbance descriptions to cull data to workers' particular needs. Second, although AMST laser scanning identifies core gaps and elevations beyond measurement and subsequently skips these intervals during spectrophotometric scanning, uneven core surfaces that prevent complete contact between the integration window and sediment surface will bias L^* toward lower values. Currently, the AMST reports only the core elevation for the integration interval and this relatively low resolution record precludes postanalysis culling of biased data. Third, surficial oxidation reactions may occur within seconds after splitting cores containing reduced sediment and these rapid reactions may be followed by additional reactions and core desiccation. Therefore, documented surface colors are not necessarily identical to pristine unoxidized sediment colors or to sediment colors subsequently observed at core repositories.

Point Magnetic Susceptibility

Archive halves containing the P/E and K/P boundary intervals were measured at 1-cm resolution on the AMST with a Bartington MS2 magnetic susceptibility meter at a sensitivity setting of 0.1 instrument units.

Smear Slide Analyses

For each smear slide, a small amount of archive-half sediment was removed with a wooden toothpick, dispersed evenly in deionized water on a 2.5 cm × 7.5 cm glass slide, and dried on a hot plate at a low setting. A drop of Norland optical adhesive was then applied, overlain by a 2.2 cm × 4.0 cm cover glass, and dried in an ultraviolet light box. Smear slides were examined with a transmitted-light petrographic microscope equipped with a standard eyepiece micrometer to assess siliclastic grain-size distribution among the clay (<3.9 μm), silt (3.9–63 μm), and sand (>63 μm) fractions. Standard petrographic techniques were employed to identify microfossil and mineral components. An area-percent technique was employed to estimate relative proportions of each grain size and type. We note two biases in smear slide analyses. First, sand-sized and larger grains (e.g., foraminifers, radiolarians, and siliclastic sand) are difficult to incorporate and often heterogeneously distributed in smear slides. Second, clay-sized sediments (e.g., clay minerals, micrite, coccoliths, and biosilica) may be difficult to distinguish and quantify and are often underestimated because of multiple layers. Smear slide data tables are included in this volume and contain sample location; whether the sample represents a dominant (D), minor (M), or accessory (A) lithology; percentages of identifiable components; and siliclastic percentages of sand, silt, and clay.

Visual Core Description and Barrel Sheets

Information from macroscopic and microscopic examination of each core section was recorded by hand on a VCD form. This information was then condensed and entered into the AppleCORE (version 8.1m) program to generate simplified core "barrel sheets." Site, hole, and depth interval (in mbsf) are given at the top of the barrel sheet, with depth and core section intervals along the left margin. Copies of the

original VCD sheets, which may contain additional and more detailed core descriptions, are available from ODP by request. Barrel sheet columns are discussed below.

Text Description

The lithologic description on each barrel sheet consists of (1) a heading listing the major sediment lithologies and (2) a detailed text description containing the descriptions and location of thin interbedded or minor lithologies, color, samples, coring conditions, and so on. Average and end-member Munsell color variations through each core, where given, represent qualitative summaries of high-resolution Minolta spectrophotometer data that are available through the Janus database.

Graphic Columns

The key for lithologic and contact symbols and bioturbation is presented in Figure F3. Lithologic symbols are arranged in the lithologic column in order of their relative abundance from left to right. Minor lithologic modifiers (10%–25% in smear slide) are represented by 20%, major lithologic modifiers (>25%–50% in smear slide) by 30%, and the primary lithology by the remaining 50%–100%. If two minor modifiers are present, each is represented by 10% within the lithologic column, and if two major modifiers are present, each is represented by 15%. Lithologic contacts ranged from gradational (hatched thick line) to sharp (solid thin line). Bioturbation is noted in a graphic column, with shading from white to black, reflecting a range from barren to abundant.

Drilling Disturbance

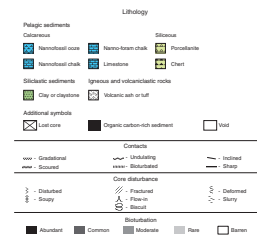
Different types of drilling disturbance were recorded graphically and textually in each barrel sheet; symbols for the type and degree of disturbance are shown in Figure F3. Drilling disturbance of relatively soft sediments (i.e., where intergrain motion was possible) was classified into four categories:

- Slightly disturbed: Bedding contacts are slightly bent.
- Moderately disturbed: Bedding contacts are extremely bowed.
- Extremely disturbed: Bedding is completely deformed and may show diapiric or minor flow structures.
- Soupy: Sediments are water saturated and show no traces of original bedding or structure.

Drilling disturbance of lithified sediments (i.e., wherein intergrain motion was not likely because of compaction, cementation, etc.) was classified into three categories:

- Fractured: Core pieces are in situ or partly displaced, but the original orientation is preserved or recognizable; pieces may be supported by drill slurry or breccia.
- Biscuited: Core pieces are from the cored interval and are probably in correct stratigraphic sequence (although they may not represent the entire section), but the original orientation is lost. Pieces are supported in drill mud.
- Breccia: Core pieces have completely lost their original orientation and stratigraphic position.

F3. Barrel sheet key, p. 44.



Samples

The positions of various core samples are indicated in the sample column as SS (smear slide), IW (interstitial water), PAL (micropaleontology), XRD (X-ray diffraction analysis), and TS (thin section). The number and location of smear slides were identified by variations and changes in macroscopic lithology; where macroscopic lithology appeared uniform, generally at least two smear slides per core were analyzed.

PHYSICAL PROPERTIES

Physical property data collected during Leg 208 provided an initial measure of the lithologic variations in the recovered core, revealing both long-term trends and high-frequency oscillations that could be interpreted in terms of the geological history of the drill sites. The information was used to (1) define major lithostratigraphic unit boundaries, (2) correlate cores from multiple holes to construct composite sections and stratigraphic splices, (3) correlate core data with downhole logging data, (4) identify effects due to sediment compaction and coring disturbance, (5) assess the relationships between signal frequencies and orbital forcing, enabling postcruise cyclostratigraphic studies, and (6) investigate the location and characteristics of major seismic reflectors.

All physical property measurements were taken on cores after they had attained room temperature, which took 2–4 hr. MS, GRA bulk density, *P*-wave velocity, NGR, and electrical conductivity were measured at high resolution on whole cores using the MST. Thermal conductivity was measured on whole cores as well. After the cores were split, additional measurements of *P*-wave velocity were conducted on the working half, and moisture and density (MAD) measurements were taken on discrete samples to calculate porosity, grain density, and bulk density. The instruments and apparatus used during Leg 208 are discussed in Blum (1997) and are outlined below.

Sampling

Multisensor Track

The MST combines five physical property sensors on an automated track that measure bulk density, MS, *P*-wave velocity (by PWL), NGR, and bulk electrical conductivity on whole-round core sections. These nondestructive measurements were taken after the cores had equilibrated to at least 18°C and before the cores were split. The MST data were sampled at the highest sampling rate possible given the time constraints of coring operations. Most cores were measured at a sample spacing of 2.5 cm, a common denominator of the distances at which the instruments are located on the track. Some intervals had to be measured at 5-cm sample spacing to accelerate core processing. The sampling periods were 4 or 5 s.

The quality of these core data and the accuracy of the nominal values were degraded if the core liner was not completely filled and/or the core was disturbed. However, general downhole trends could still be used for core-to-core and core-to-well logging correlation in most cases.

Split-Core Working Half

On every other core section (nominal sampling interval of 3 m) a sound velocity measurement was taken using the *P*-wave velocity sensor 3 on the Hamilton Frame probe (PWS3). A sediment sample of ~10 cm³ was subsequently extracted from the PWS3 measurement location and subjected to MAD measurements. An additional small core sample was taken from the same location and passed to the chemistry laboratory for the determination of calcium carbonate concentration.

Split-Core Archive Half

Two instruments are mounted on the AMST for the measurement of color reflectance and MS. Both instruments are moved across the track by stepper motors and landed on the split-core surface at predetermined sampling intervals for the measurements. Freshly split cores were covered with clear plastic wrap before being placed on the AMST to protect the probes from being soiled. The AMST runs a laser scan first to determine surface roughness and to allow the skipping of intervals where the core surface is well below or above the level of the core liner. However, the AMST cannot recognize relatively small cracks or disturbed areas of core. Thus, AMST data may contain spurious measurements that should, to the extent possible, be edited out of the data set before use.

Color reflectance was measured on the archive halves after the cores were described and before they were measured for magnetic intensity, inclination, and declination in the cryogenic magnetometer. Sample spacing was 2.5 cm throughout the leg, except for critical intervals such as the P/E and K/P boundary intervals, which were measured at a spacing of 1 cm.

MS was measured using the “point sensor” on selected intervals. These measurements are very slow with the available equipment; therefore, only the critical intervals were measured. The sample spacing was usually 1 cm for those intervals.

Description of Physical Properties Measured

Magnetic Susceptibility

Whole-core MS was measured with a Bartington MS2C meter using an 80-mm internal diameter sensor loop (88-mm coil diameter). The measurements were routinely corrected for temperature drift in the loop by using two reference measurements at the beginning and end of a section run and assuming constant change during the time a core section is measured. The data were stored in the ODP Janus database as raw instrument units and were not corrected for changes in sediment volume. To obtain SI units, these instrument units need to be multiplied by $\sim 0.68 \times 10^{-5}$, although exact conversions are best done using control measurements on discrete samples, correcting for the actual core volume measured (Blum, 1997).

Gamma Ray Attenuation Bulk Density

GRA bulk density measurements allow estimation of wet bulk densities by measuring the attenuation (Compton scattering) of gamma radiation passing through the unsplit core sections. GRA bulk density data are most reliable in undisturbed cores and can often be directly corre-

lated with the downhole density logs. In disturbed cores, GRA density is underestimated. Calibration was performed using a series of water/aluminum core segments.

Compressional Wave Velocity

P-wave velocity was estimated using two measurement devices: the PWL on the MST and the PWS3 system (essentially a “Hamilton Frame”) on the split core. Both systems send 500-kHz *P*-wave pulses through the core and the core liner at a frequency of 1 kHz. The transmitting and receiving transducers are aligned perpendicular to the core. Displacement transducers monitor the separation between the *P*-wave transducers, and the distance is used to convert traveltime into velocity after correcting for the liner. Good coupling between the liner and the core is crucial for obtaining reliable measurements. Calibration of the displacement transducers is performed using a series of acrylic blocks of known thicknesses. The *P*-wave traveltime and measurement of electronic delay within the PWL circuitry were calibrated using a plastic bag filled with distilled water. The bag was manipulated to sit between the transducers at varying distances. Repeated measurement of *P*-wave velocity through a core liner filled with distilled water was used to check the calibration validity. Velocity data were not corrected for in situ temperature and pressure. These corrections can be made using the relationships outlined in Wyllie et al. (1956), Wilson (1960), and Mackenzie (1981).

Natural Gamma Radiation

NGR emissions result from the decay of radioactive isotopes and were measured in the laboratory by scintillation detectors. Results were reported in counts per second, which can then be compared qualitatively with the downhole logging data. NGR calibration was performed at the beginning of the leg.

Non-Contact Resistivity Sensor

The Non-Contact Resistivity (NCR) system measures the electrical conductivity of sediments and rocks through the core liner. Combination logs of resistivity and density provide pertinent lithologic information (grain size/permeability/tortuosity) that cannot be achieved with other nondestructive measurements. The NCR technique operates by inducing a high-frequency magnetic field in the core, from a transmitter coil, which in turn induces electrical currents in the core that are inversely proportional to the resistivity. Very small magnetic fields regenerated by the electrical current are measured by a receiver coil. To measure these very small magnetic fields accurately, a difference technique has been developed that compares the readings generated from the measuring coils to the readings from an identical set of coils operating in air. This technique provides the requisite accuracy and stability required. Resistivities between 0.1 and 10 Ωm can be measured at spatial resolutions of 2 cm along the core. Resistivity measurements vary with core temperature and should be obtained in a stable temperature environment for best results. Calibration is achieved by filling the core liner with water of known salinities (and hence known resistivities) and normalizing the core measurement results with the reference measurements.

Moisture and Density

Porosity, grain density, and bulk density of 10-cm³ sediment specimens were calculated from measurements of wet and dry sediment mass and dry sediment volume. Wet and dry sample mass was determined with a reproducibility of $\pm 3\%$ standard deviation using a Scientech electronic balance that compensates for the ship's motion. Wet sample mass was measured immediately after collection. Dry sample mass and dry sediment volume were measured after the samples had been dried in a convection oven at $105^\circ \pm 5^\circ\text{C}$ for 24 hr and allowed to cool in a desiccator. Dry sample volume was determined using a Quantachrome penta-pycnometer, a helium-displacement pycnometer. Sample volumes were determined at least five times, until readings were consistent (volume error within 1%). The principles and calculations are summarized in Blum (1997).

Thermal Conductivity

Thermal conductivity is the measure of a material's ability to transmit heat by molecular conduction. Thermal conductivity and temperature measurements of sediments and rock sections are used to determine heat flow. Heat flow is not only characteristic of the material but is also an indicator of type and age of ocean crust and fluid circulation processes at shallow and great depths. Thermal conductivity was measured in soft sediments using the TK04 measurement system (see Blum, 1997), with the needle-probe method in full-space configuration (Von Herzen and Maxwell, 1959), after the core had equilibrated to ambient temperature. The full-space needle, containing a heater wire and calibrated thermistor, was inserted into the sediment through a small hole drilled into the core liner. Measurement errors are 5%–10%.

BIOSTRATIGRAPHY

Preliminary age assignments were based on biostratigraphic analyses of calcareous nannofossils and planktonic foraminifers. Core catchers from all holes at each site were examined for calcareous nannofossils and planktonic foraminifers, whereas for benthic foraminifers, usually only core catcher samples from the hole with the deepest penetration were used. In addition to core catcher samples, one to six samples per core (sample spacing = 0.25–1.5 m) were examined for shipboard determination of stratigraphic positions of nannofossil datums. More detailed sampling was conducted across critical intervals such as the P/E and K/P boundaries. The preservation, abundance, and zonal assignments for each microfossil group have been recorded in the stratigraphic site summary sheets and entered into Excel spreadsheets (see the [“Supplementary Material”](#) contents list).

Zonal Schemes and Taxonomy

Calcareous Nannofossils

The zonal scheme of Bukry (1973, 1975) with the CN and CP zonal code notation as added by Okada and Bukry (1980) was used for Cenozoic calcareous nannofossil biostratigraphy. These zonations provide a general framework for the biostratigraphic classification of mid- to low-latitude nannofossil assemblages and are correlated with Martini's

(1971) NN and NP nannofossil zones (Fig. F4). In the lower Eocene, the Zone CP11/CP10 boundary was not recognized because its marker species, *Toweius crassus*, was recorded in older sediments (within Subzone CP9b) at several Leg 208 sites. The lower Paleocene marker species *Ellipsolithus macellus*, used in the standard zonations, is very rare in the lower part of its range and was not used for biostratigraphic classification. Nannofossil taxonomy follows that of Perch-Nielsen (1985). Cenozoic biostratigraphic events, including Okada and Bukry's (1980) zonal indicators and additional markers, are listed in Table T1. Age estimates of biohorizons are all adjusted to the timescale of Leg 208 (see "Age Model and Mass Accumulation Rates," p. 33).

The zonal scheme of Sissingh (1977; CC zones), as modified by Perch-Nielsen (1985) and Roth (1978; NC zones), was used for the Upper Cretaceous. These zonations provide a general framework for the biostratigraphic classification of mid- to low-latitude nannofloral assemblages (Table T1). Cretaceous nannofossil taxonomy follows that is used in Perch-Nielsen (1985) and Bown (1999). Numerical ages reported by Erba et al. (1995) have been adopted for the Maastrichtian events (Table T1).

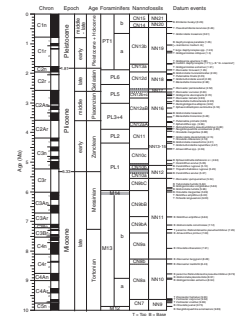
Planktonic Foraminifers

The tropical planktonic foraminiferal zonal scheme for the Cenozoic follows Berggren et al. (1995a, 1995b) (Fig. F4; Table T2). For the Miocene, the zonation for transitional austral regions was used in addition to the tropical zonation because of the overall absence of several tropical/subtropical marker species (Berggren et al., 1995a, 1995b). Age estimates of the datums are all adjusted to the timescale of Leg 208 (see "Age Model and Mass Accumulation Rates," p. 33). Numerical ages and references for the Cenozoic planktonic foraminiferal datum levels are presented in Table T2. Cenozoic taxonomic concepts selectively follow Postuma (1971), Kennett and Srinivasan (1983), Bolli and Saunders (1985), Toumarkine and Luterbacher (1985), Spezzaferri and Premoli Silva (1991), Chaisson and Leckie (1993), Spezzaferri (1994), Chaisson and Pearson (1997), Pearson and Chaisson (1997), and Olsson et al. (1999). The zonation used for Cretaceous planktonic foraminifers is based on the tropical zonal schemes of Caron (1985).

According to the *Astronomical Tuned Neogene Timescale 2004* (Lourens et al., in press), the top of the *Hirsutella cibaoensis* range of 4.16 Ma falls within Zone PL2 and can therefore not be used to define Subzone PL1a within the lowermost Pliocene (Fig. F4). Furthermore, a number of key taxa used in the standard tropical biozonation for the Neogene are either extremely rare or absent in Leg 208 sites, thereby negating their stratigraphic utility. Some of these ecologically excluded Neogene taxa are *Globigerinoides fistulosus*, *Globorotalia tumida*, *Menardella exilis*, *Menardella pertenuis*, *Menardella multicamerata*, *Pulleniatina primalis*, and *Pulleniatina spectabilis*. Later members of the biostratigraphically useful *Fohsella* lineage are missing from the middle Miocene as well. The absence of these marker taxa limits biostratigraphic resolution within the Neogene sections from Walvis Ridge. For instance, Zones M2 and M3 of the lower Miocene could not be differentiated because of the absence of the marker species *Globigerinatella insueta*.

Ecological exclusion of tropical marker species occurs within the Paleogene as well. Moreover, intervals of intense dissolution and extensive reworking throughout much of the middle Eocene through Oligocene have disrupted the Paleogene stratigraphy, and species of the

F4. Calcareous nannofossil and planktonic foraminiferal zonation, p. 45.



T1. Cenozoic and Mesozoic calcareous nannofossil datums, p. 52.

T2. Cenozoic and Mesozoic planktonic foraminiferal datums, p. 54.

marker taxon *Hantkenina* spp. are rare or absent. The marker *Cribohantkenina inflata* is not present in any of the uppermost Eocene sections, making it impossible to differentiate Zones P16 and P17. Hence, the standard biozonation of Berggren et al. (1995a, 1995b) has been amended by omitting Zone P17 (Fig. F4). The absence of such dissolution-susceptible taxa as *Planorotalites palmerae* and *Hantkenina nuttalli* precludes direct identification of Zones P9 and P10, and alternative biostratigraphic criteria are used. To this end, Zone P9 is approximated by an acme in the relative abundance of *Morozovella caucasica*. Scarcity of *Morozovella formosa* and *Morozovella velascoensis* within well-preserved assemblages from the lower Eocene is evidence for atypical environmental conditions in this subtropical area.

The boundary between Zone P5 and Subzone P6a could not be determined with confidence at Leg 208 sites. This boundary is defined by the uppermost occurrence of *M. velascoensis* (54.31 Ma), which occurs above the benthic foraminiferal extinction event (BEE) at the base of the carbon isotope excursion (CIE) marking the P/E boundary (55 Ma) (Norris and Röhl, 1999; Luterbacher et al., 2000). At all Leg 208 sites, the uppermost occurrence of *M. velascoensis* was observed close to the BEE, with only rare and discontinuous occurrences above that event. The last appearance datum of *M. velascoensis* is thus diachronous, and the species has a shorter range at higher latitudes. We used the recalibrated numerical ages (Norris and Röhl, 1999; Röhl et al., 2000, 2003) within a narrow stratigraphic interval bracketing the P/E boundary (55.0 Ma). For the Upper Cretaceous, we used the numerical age for zonal boundaries as given in Erba et al. (1995), Bralower et al. (1995), and Premoli Silva and Sliter (1999) (Table T1).

Benthic Foraminifers

We used the depth zonation of van Morkhoven et al. (1986) for benthic foraminifers (Table T3).

Benthic generic classification follows mainly Loeblich and Tappan (1988), except where modified by Hayward (2002) for uniserial taxa. Species classification mainly follows Boltovskoy (1978), Tjalsma and Lohmann (1983), Thomas (1985, 1990), van Morkhoven et al. (1986), Boltovskoy and Boltovskoy (1989), various papers on agglutinated foraminifers in Hemleben et al. (1990), Müller-Merz and Oberhänsli (1991), Boltovskoy and Watanabe (1993), Boltovskoy et al. (1995), Nomura (1995), Thomas and Shackleton (1996), Schmiedl et al. (1997), Widmark (1997), and Alegret and Thomas (2001).

Because of time constraints aboard the ship, assemblages could be examined only superficially and not enough specimens could be counted per sample for full evaluation. Deep-sea benthic foraminifers are diverse, and at least 200 specimens must be counted for Neogene assemblage evaluation (300 for Paleogene assemblages). Only ~50–100 specimens per sample could be counted, and the paleodepth estimates, ranges of taxa, and remarks on dominance and species richness are thus preliminary.

Critical Intervals

Eocene/Oligocene Boundary

The lower Oligocene is zoned in greatest detail by calcareous nannofossils (Fig. F4), although the Eocene/Oligocene (E/O) boundary is rec-

T3. Benthic foraminifer depth zones, p. 57.

ognized by the last occurrence (top [T]) of the planktonic foraminiferal genus *Hantkenina*. The E/O boundary is present within uppermost Chron C13r at the planktonic foraminifer Biozone P16/P18 boundary and within the calcareous nannofossil Subzone CP16a (NP21).

Calcareous nannofossil datum levels within 2 m.y. of the E/O boundary (33.7 Ma) include the uppermost occurrence (T) of *Reticulofenestra umbilicus* (31.7 Ma), the T of *Ericsonia formosa* (32.9 Ma), and the onset (bottom [B]) of the acme of *Ericsonia obruta* (33.7 Ma). The bottom of the acme of *E. obruta* in the mid- to low latitudes seems to approximate the E/O boundary. The uppermost Eocene is easily determined by the presence of the rosette-shaped discoasterids *Discoaster saipanensis* (T at 34.0 Ma) and *Discoaster barbadiensis* (T at 34.2 Ma). The boundary interval should be constrained between the T of *D. saipanensis* and *D. barbadiensis* and the T of *E. formosa*.

Among the planktonic foraminifers, the tops of the stratigraphic ranges of *Globigerinatheka* spp. (~34.3 Ma) and the *Turborotalia cerroazulensis* lineage (~33.8 Ma) can be used to approximate the E/O boundary. Unfortunately, the genera *Hantkenina* and *Turborotalia* are particularly susceptible to dissolution. Hence, the top of the thick-shelled globigerinathekids is used to approximate the E/O boundary. In addition, the top of the genus *Pseudohastigerina* (32.0 Ma) delimits the top of the lowermost planktonic foraminiferal zone in the Oligocene.

Paleocene/Eocene Boundary

The P/E boundary has been placed at the planktonic foraminiferal Zone P5/P6 boundary in the middle part of calcareous nannofossil Zone NP10 (CP9a) (Aubry et al., 1996). The International Subcommission on Paleogene Stratigraphy on the Criterion for the Recognition of the Paleocene/Eocene Boundary redefined this boundary and placed it at the base of the CIE. The CIE, and by definition the P/E boundary, occurs at the same level as the top of the benthic foraminifer *Stensioeina beccariiiformis*, within reversed Magnetochron C24r (Luterbacher et al., 2000). From a biostratigraphic point of view, the P/E boundary falls within planktonic foraminiferal Zone P5 and in the upper part of calcareous nannofossil Zones CP8 and NP9.

The P/E boundary can be approximated by a series of calcareous microfossil datum levels (Fig. F4). These events include a major extinction event among benthic foraminifers at bathyal to abyssal depths (including *S. beccariiiformis*, *Aragonia velascoensis*, *Paralabamina lunata*, *Paralabamina hillebrandti*, and *Osangularia velascoensis*), which has been correlated precisely to the base of the CIE (e.g., Thomas and Shackleton, 1996). At all Leg 208 sites, the T of *S. beccariiiformis* occurs directly below the base of a pronounced clay layer. Our data thus do not agree with Tjalsma and Lohmann (1983), who described the last occurrence of this species as occurring earlier at abyssal depths.

The postextinction interval can be recognized by the presence of low-diversity, small, and thin-walled foraminifers on Walvis Ridge dominated by *Nuttallides truempyi* and various abyssaminid taxa (Boltovskoy and Boltovskoy, 1989; Müller-Merz and Oberhänsli, 1991; Thomas and Shackleton, 1996). In noncarbonate sequences, this postextinction interval can be recognized by the dominance of *Glomospira* spp., the so-called earliest Eocene “*Glomospira* event” in agglutinated assemblages (Kaminski et al., 1996; Galeotti et al., in press).

The P/E boundary can also be identified by the presence of the planktonic foraminifer “excursion fauna” that includes *Acarinina africana*, *Ac-*

arinina sibaiaensis, and *Morozovella allisonensis* (Kelly et al., 1996, 1998). The planktonic foraminifers *Pseudohastigerina wilcoxensis* and large specimens of *Chiloguembelina wilcoxensis* have lowermost occurrences (bases) close to the boundary as well (Speijer and Samir, 1997). Furthermore, the P/E boundary is typically associated with a marked increase in the relative abundance of the genus *Acarinina* (Kelly, 2002). The P/E boundary is followed by the T of *M. velascoensis* (~54.31 Ma) (Norris and Röhl, 1999).

The B of *Rhombaster cuspis*, the oldest representative of the *Rhombaster-Tribrachiatus* lineage, occurs at the base of the clay-rich interval. A decrease in the relative abundance of the calcareous nannofossil genus *Fasciculithus* together with an increase in abundance of *Zygrhablithus* spp. is recorded just above the P/E boundary. We do not use the B of *Campylosphaera eodela*, the marker for the lower boundary of Subzone CP8b, because specimens of *C. eodela* occur far below the lowermost occurrence of *Discoaster multiradiatus* (the base of Biozone CP8) (Bralower and Mutterlose, 1995). All these biostratigraphic events are present in the long interval of reversed polarity, Chron 24r. According to Cande and Kent (1995), Chron C24r has a duration of 2.557 m.y. Recent cyclostratigraphic work (Norris and Röhl, 1999; Röhl et al., 2000, 2003) indicates that the base of the CIE, and therefore the P/E boundary, occurred ~1 m.y. after the end of Chron C25n, at 55.0 Ma. We have used this age for the P/E boundary in the Leg 208 timescale.

Cretaceous/Paleogene Boundary

The K/P boundary is marked by one of the largest mass extinctions in Earth history. The extinction level is about halfway through Magnetochron C29r and occurred ~250 k.y. before the magnetic reversal at the base of Chron C29n. The top of the Maastrichtian is recorded in the extinction of ~95% of planktonic foraminifers, including the globotruncanids, rugoglobigerinids, and the large serially coiled planktonic foraminifers. The nearly exclusive presence of minute planktonic foraminifers (which are typically <63 µm in diameter) is characteristic of the lowermost Paleogene (Danian) sediments above the K/P boundary. The Danian species include *Parvulorugoglobigerina eugubina*, *Guembelitra cretacea*, and *Heterohelix globulosa*. Previous zonations have identified Zone P0 as dominated by *G. cretacea*, between the K/P boundary and the lowermost appearance of *P. eugubina* (~64.97 Ma). However, re-examination of the classic K/P boundary section and Global Standard Stratotype Section and Point at El Kef, Tunisia, has demonstrated that rare specimens of *P. eugubina* are present directly above the extinction level of the Cretaceous foraminifers, suggesting that Zone P0 reflects an increase in abundance of *P. eugubina* rather than its evolutionary lowermost appearance (Norris et al., 1999).

Calcareous nannofossils also display a significant extinction across the K/P boundary. The lowermost Danian is characterized by an increase in abundance of *Thoracosphaera* spp. and the B of *Biantholithus sparsus* and *Cyclagelosphaera reinhardtii*. The K/P boundary is also bracketed by the B of *Cruciplacolithus primus* (64.8 Ma) and *Cruciplacolithus tenuis* (64.5 Ma) above the boundary and the lowermost occurrence (base) of *Micula prinsii* (65.4 Ma) below the boundary.

Benthic foraminifers did not suffer significant extinction at the K/P boundary but in many locations show short-lived changes in assemblage composition (Culver, 2003).

Methods

Calcareous Nannofossils

Calcareous nannofossils were examined in smear slides using standard light-microscope techniques under crossed nicols and transmitted light at 1000× magnification. The following abbreviations were used to describe nannofossil preservation:

- G = good preservation (little or no evidence of dissolution and/or recrystallization; diagnostic characteristics fully preserved).
- M = moderate preservation (dissolution and/or secondary overgrowth; partially altered primary morphological characteristics; most specimens were identifiable to the species level).
- P = poor preservation (severe dissolution, fragmentation, and/or overgrowth; primary morphological characteristics largely destroyed; specimens often could not be identified at the species and/or generic level).

The total abundance of calcareous nannofossils in a smear slide was estimated as follows:

- A = abundant (>100 specimens in a field of view).
- C = common (2–100 specimens in a field of view).
- B = barren.

Abundances of calcareous nannofossil taxa were estimated, and their abundance levels were recorded as follows:

- A = abundant (the taxonomic category constitutes >10 specimens per field of view).
- C = common (the taxonomic category constitutes 2 to 10 specimens for each field of view).
- F = few (the taxonomic category ranges from <2 specimens for each field of view to 1 specimen for every five fields of view).
- R = rare (the taxonomic category constitutes <1 specimen for every five fields of view).
- RR = very rare (the taxonomic category constitutes <1 specimen for one track).
- P = present (abundance is not evaluated).
- B = barren.

Foraminifers

Benthic and planktonic foraminifers were extracted from unlithified ooze by washing samples over a 63- μm sieve. More indurated samples were broken into small (<1-cm diameter) pieces, soaked in a 3% solution of hydrogen peroxide with a small amount of Calgon, warmed on a hot plate, and then washed with tap water over a 63- μm sieve. A smaller sieve size (38 μm) was used for stratigraphic intervals in which key marker taxa are diminutive (e.g., lowermost Danian and parts of the lower Eocene). All samples were dried in a low-temperature oven at ~50°C.

Species identification was generally made in the >63- μm size fraction. Because of time constraints imposed by ongoing coring, the relative abundances of foraminiferal taxa were estimated semiquantita-

tively. In some instances, only presence/absence data were compiled for major marker species, distinctive morphotypes, and/or dominant species in a sample.

The preservation status of the planktonic and benthic foraminifers was estimated as follows:

- E = excellent (glassy).
- G = good (little evidence of overgrowth, dissolution, or abrasion).
- M = moderate (calcite overgrowth, dissolution, or abrasion common but minor).
- P = poor (substantial overgrowth, dissolution, or fragmentation).
- B = barren (no planktonic foraminifers present).

The abundance of planktonic foraminifers in a given sample is expressed as follows:

- A = abundant (>63- μ m size fraction dominated by planktonic foraminifers).
- C = common (moderate amounts of planktonic foraminifers in >63- μ m size fraction).
- R = rare (few planktonic foraminifers in >63- μ m size fraction).
- B = barren (no planktonic foraminifers in >63- μ m size fraction).

The abundance of planktonic and benthic foraminiferal species was expressed as follows:

- a = abundant (>30% of the assemblage).
- c = common (10%–30% of the assemblage).
- f = frequent (~2%–10% of assemblage).
- r = rare (only a few specimens per picking tray).

The abundance of benthic foraminifers was expressed as follows (P/B = number of planktonic foraminifers/number of benthic foraminifers):

- R = rare (P/B > ~100).
- F = few (P/B = ~75–100).
- C = common (P/B = ~15–75).
- A = abundant (P/B < ~15).

PALEOMAGNETISM

The primary objective of the shipboard paleomagnetic study was to produce a detailed polarity stratigraphy whenever possible. At selected sites, attempts were also made to characterize the magnetic mineralogy and magnetic properties of the sediments and to make preliminary estimates of relative paleointensity. These objectives were achieved through measurements of natural remanent magnetization (NRM) and alternating-field (AF) demagnetization of all archive halves, as well as through more detailed measurements of pilot discrete samples taken from the working half.

The conventional right-handed ODP coordinate system was used throughout (+z = downcore; +x = vertical upward from the split surface of the archive half). Orientations of APC cores were recorded using the Tensor tool (Tensor Inc., Austin, Texas). The Tensor tool consists of a three-axis fluxgate magnetometer that records the orientation of the

double lines scribed on the core liner with respect to magnetic north. The critical parameters for core orientation are the inclination angle (typically $<2^\circ$) and the angle between magnetic north and the double line on the core liner, known as the magnetic toolface angle.

Instrumentation

Half-core measurements were made using the shipboard long-core cryogenic magnetometer (2G Enterprises model 760R) equipped with an in-line, automated AF demagnetizer. The pickup coils of the magnetometer have a width at half height of <10 cm for all three axes, although they may sense a magnetization over an interval of 30 cm. The background noise on the magnetometer was measured to be less than $\sim 5 \times 10^{-11}$ Am² under normal conditions. The noise level increased by nearly three orders of magnitude during pipe trips and became highly periodic. This problem was especially pronounced on the y-axis, whereas the z-axis appeared nearly unaffected. These levels should not significantly affect most of the half-core measurements, which were made under normal conditions and typically had moments greater than 10^{-7} Am². However, measurements of more weakly magnetized sediments with moments less than 5×10^{-8} Am² could be affected by this noise.

Isothermal remanent magnetization (IRM) was imparted with an ASC Scientific model IM-10 impulse magnetizer. Whole-core measurements of low-field susceptibility were conducted on the MST system (see “[Multisensor Track](#),” p. 11, in “Sampling” in “Physical Properties”).

Measurements and Procedures

Measurements of remanent magnetization were carried out for all archive halves at 5-cm intervals with 10-cm-long headers and trailers. Time permitting, cores were also AF demagnetized at 10 and 15 mT to isolate the characteristic remanent magnetization. The low maximum peak demagnetization level ensured that the archive halves remained useful for shore-based studies. Sections that had clearly suffered from severe drilling-related disturbance were either not measured at all or were measured only at 15 mT. In an attempt to improve the quality of the data in the soft carbonate sediments, many of the cores from Hole 1266C were measured and demagnetized to 15 mT as whole rounds (see “[Paleomagnetism](#),” p. 18, in the “Site 1266” chapter). This resulted in the demagnetization (up to 15 mT) of the working-half sections of these cores (Table [T4](#)). The working halves of several other sections were also demagnetized to 15 mT as part of an experiment to determine the source of bias in the declination data (Table [T4](#)).

A small set of discrete samples processed aboard the ship were AF demagnetized in steps. Following AF demagnetization, several samples were additionally imparted an anhysteretic remanent magnetization at 100 mT in a 50- μ T bias field and were again stepwise AF demagnetized. An IRM was then progressively acquired, followed by a stepwise back-field IRM to determine the coercivity of remanence.

Drill String Overprint

A strong drilling overprint directed in the vertical down (+z) direction was observed at all sites, regardless of the use of a nonmagnetic

[T4](#). Demagnetization of working halves and core sections, p. 58.

core barrel. In most cases this overprint appears to be removed by a 10-mT demagnetization. In addition to the vertical overprint, a strong bias in the archive-half declination data toward 0° in the ODP coordinate system was also observed at all sites (Fig. F5A). This phenomenon has been previously observed in soft sediments and has been attributed to a radially directed drilling overprint (Fuller et al., 1998). This bias is not removed by demagnetization to 15 mT (Fig. F5A, F5C) and results in random distribution of declinations after correcting the core data with the directional information from the Tensor tool (Fig. F5B). The problem may be at least partially (though by no means fully) mitigated by the measurement of whole cores (Fig. F5C, F5D), which is consistent with a radial component of magnetization.

Sediment Core Surface Smoothing and Data Quality

The surface of the archive halves was routinely smoothed or scraped by the sedimentologists prior to measurement on the pass-through magnetometer. Questions were raised as to whether this smoothing process was contributing to the erratic or poorly defined inclination data observed at many sites. To determine whether the smoothing was affecting the magnetization of the soft-sediment split cores, several sections were measured before and after smoothing. It was determined that smoothing most likely does not affect the magnetization of the archive halves (see “Paleomagnetism,” p. 20, in the “Site 1265” chapter for test results and further discussion).

Magnetostratigraphy

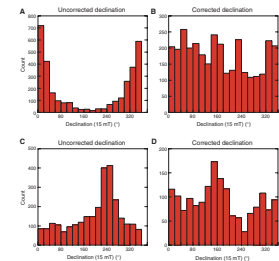
Preliminary reversal age assignments were based on the half-core inclination data after the removal of a low-coercivity overprint. The top 50 cm of each core was routinely ignored for this purpose because of the possible presence of drill string contamination and coring deformation. Data within 5 cm of section ends were also ignored because of edge effects. The timescale used for age assignments was chosen to provide a common age model for both biostratigraphic and magnetostratigraphic observations. This scale combines the astronomically calibrated model of Lourens et al. (in press) to the Oligocene/Miocene (O/M) boundary, the astronomically tuned ages of H. Pälike et al. (pers. comm., 2003) from the O/M boundary to the base of Chron C11n, and the ages of Cande and Kent (1995) for older periods (Table T5).

We also give all chron ages as in Cande and Kent (1995). Magnetostratigraphic interpretations at many sites were hampered by poor data quality. In addition to the drill string overprint (see above), the poor data quality is attributed to unstable or weak NRM in the sediments, deformation caused by the drilling and/or core splitting procedures, and possibly spurious directional changes induced by abrupt intensity changes (Parker and Gee, 2002).

Preliminary Paleointensity Analyses

At selected sites, preliminary estimates of relative paleointensity were made by normalizing the half-core NRM data by susceptibility. This normalized depositional remanent magnetism record is intended to give a first-order approximation of relative paleointensity until a more thorough postcruise analysis can be conducted.

F5. Bias in measured declination data, p. 50.



T5. Timescale used for magnetostratigraphic age assignments, p. 59.

GEOCHEMISTRY

Gas Analyses

Concentrations of light hydrocarbon gases methane (C_1), ethane (C_2), and propane (C_3) were monitored for safety and pollution prevention. The C_1/C_2 ratio is particularly important for indicating potential petroleum occurrences; sediments rich in organic carbon (C_{org}) commonly have a ratio of >1000 , whereas values <200 may indicate potential petroleum generation related to increasing depth and temperature (Pimmel and Claypool, 2001).

The standard procedure described by Pimmel and Claypool (2001) was followed for sampling headspace gases in each core. Immediately after core retrieval on deck, a $\sim 5\text{-cm}^3$ sediment sample was collected using a borer tool, placed in a 20-cm^3 glass serum vial, and sealed immediately in the laboratory with a septum and metal crimp cap. For consolidated or lithified samples, chips of material were placed in the vial and sealed. Prior to gas analyses, the vial was heated at 70°C for 30 min.

For volatile hydrocarbon analysis, a 5-cm^3 subsample of the headspace gas was extracted from each vial using a 5-cm^3 glass gas syringe and injected into a Hewlett-Packard (HP) 6890 gas chromatograph (GC3). The GC3 is equipped with a sample loop, an $8\text{ ft} \times 1/8$ in stainless steel column packed with divinylbenzene and N-vinyl-2-pyrrolidinone (HayeSep R), a flame ionization detector, and an electropneumatic control (EPC) system. Helium was used as the carrier gas. HP Chemstation software was used for data acquisition and processing. Chromatographic responses were calibrated using commercial standards (Scotty II Analyzed Gases, Scott Specialty Gas Co.), and the results were reported in parts per million by volume (ppmv [$\mu\text{L}/\text{L}$]).

Interstitial Water Sampling and Chemistry

Shipboard interstitial water analyses were performed on 5- to 10-cm-long whole-round sections that were cut immediately after the core arrived on deck. In most cases, one whole-round section was taken from the lower third of each core. To avoid the destruction of critical intervals, whole-round sections were not removed from cores adjacent to such intervals as determined by shipboard biostratigraphy. Details of the sampling resolution are described in the individual site chapters of this volume. After extrusion from the core liner, the surface of each whole-round section was scraped with a spatula to remove potential contamination. Interstitial waters were collected using a titanium squeezer, modified after the standard ODP stainless steel squeezer of Manheim and Sayles (1974). Pressure up to 205 MPa (30,000 psi) was applied using a hydraulic press. Pore waters were passed through pre-washed Whatman number 1 filters fitted above a titanium screen and subsequently extruded through a $0.45\text{-}\mu\text{m}$ polycarbonate filter into a plastic syringe attached to the bottom of the squeezer assembly. Samples for shipboard analysis were stored in plastic vials pending analysis. Aliquots for future shore-based analyses were placed in glass ampules or plastic tubes and heat-sealed.

Interstitial water samples were routinely analyzed for salinity as total dissolved solids with a Goldberg optical handheld refractometer. The pH and alkalinity were determined by Gran titration with a Brinkmann pH electrode and a Metrohm autotitrator. Dissolved chloride was determined by titration with AgCl. Sulfate (SO_4^{2-}) content was quantified by

ion chromatograph. Lithium (Li^+), boron (H_3BO_3), sodium (Na^+), magnesium (Mg^{2+}), silicon ($\text{Si}(\text{OH})_4$), potassium (K^+), calcium (Ca^{2+}), manganese (Mn^{2+}), iron (Fe^{2+}), zinc (Zn^{2+}), strontium (Sr^{2+}), and barium (Ba^{2+}) concentrations were determined by inductively coupled plasma–atomic emission spectroscopy (ICP-AES) following the general procedure outlined by Murray et al. (2000). In preparation for analysis by ICP-AES, aliquots of interstitial waters were acidified with nitric acid (HNO_3). These acidified samples were then diluted to a ratio of 1:10 for the analysis of minor elements and to a ratio of 1:50 for the analysis of major elements (Na, Mg, K, and Ca), with 2.5% HNO_3 doped with 10 ppm of Y for internal standardization.

The chemical data for interstitial waters are reported in molar units. The reproducibility of results, determined by multiple analyses of International Association for the Physical Sciences of the Ocean (IAPSO) standard seawater (alkalinity, Cl^- , Na^+ , Mg^{2+} , K^+ , and Ca^{2+}), a synthetic seawater standard (trace element ICP-AES determinations), or through the use of a calibration curve (SO_4^{2-}), is available in Table T6. In addition, one interstitial water Sample 208-1262A-15H-5, 140–150 cm, was analyzed repeatedly for both major and minor elements throughout the duration of shipboard ICP-AES analyses and the reproducibility for this consistency standard is given in Table T6. The consistency standard was chosen because it contained representative concentrations of all elements analyzed and because a substantial volume was available.

Inductively Coupled Plasma–Atomic Emission Spectroscopy

The range of concentrations to be included in the suite of synthetic seawater standards was determined following consideration of concentration ranges in seawater (IAPSO certified values or Burton, 1996) and the Li, Si, Ca, and Sr data presented for interstitial water samples from Deep Sea Drilling Project Leg 74 (Gieskes et al., 1984). Li, Si, and especially Sr were found to be enriched in interstitial water samples from Leg 74 with respect to seawater. This was also the case for Ca, which was found to be as concentrated as 76.5 mM in material from the bottom of Hole 528 compared with a seawater concentration of 10.55 mM. Therefore, it was necessary to dope the IAPSO seawater used to calibrate ICP-AES analyses of the major elements (Mg, Na, K, and Ca) with CaCO_3 to ensure that the potential range of Ca concentrations in the interstitial water samples would be bracketed. To assess the potential contribution of contaminants in the CaCO_3 powder, a blank of CaCO_3 powder was dissolved in 2.5% nitric acid (the matrix to be used in the dilution of standards and samples). Salinity is correlated to total dissolved solids and is likely to affect the intensities measured by the ICP-AES, so care was taken to ensure the calibration standards were salinity matched to the samples. Specifically, for the calibration of Mg, K, and Ca analyses, the IAPSO seawater was diluted with 2.5% HNO_3 and a NaCl solution to ensure constant salinity of 35 g/kg. For the calibration of Na, it was necessary to prepare dilutions of the IAPSO seawater with 2.5% HNO_3 to obtain standards of differing Na concentration.

The synthetic seawater standards for standardization of the trace and minor element signals were doped with NaCl to maintain a salinity of 35 g/kg, matching that of the pore water samples. Nitric acid doped with NaCl to 35 g/kg was run as a blank for the synthetic seawater standards, and plain nitric acid blanks were used as the blank for the samples. The trace elements that were usually analyzed during previous legs (Li, B, Si, Mn, Fe, Sr, and Ba) were included in the synthetic seawater

T6. Interstitial water geochemistry quality control results, p. 60.

standards. Zn at concentrations between 0.1 and 4.6 μM was also added to quantify the abundance of Zn in the interstitial water samples. Zn pore water data was collected for Sites 1262–1265 but failed to display any significant downhole trends and was characterized by stochastic noise associated with a large and variable blank. Thus, shipboard pore water Zn analyses were considered unreliable and were discontinued. The concentrations of Mn and Fe in the synthetic standards were adjusted to be above detection limits but at very low concentrations to ensure that if natural samples were encountered with low Fe and Mn contents, they would be bracketed by standard calibration points. Even so, the range of Mn and Fe concentrations encountered in Leg 208 pore waters was large and in some samples the concentrations were about twice that of the most concentrated standard. However, as the calibration curves were linear (giving r^2 values of >0.99), the calibrations were considered robust enough to quantify unknowns above their range.

Sediment Elemental Analysis

Freeze-dried and powdered squeeze cake sediment samples with CaCO_3 contents $>80\%$ from Sites 1263 and 1264 were leached using dilute ($\sim 0.1\%$) nitric acid in an attempt to dissolve the carbonate fraction. The leachate was analyzed for the same ions as the interstitial water samples using ICP-AES with the exception of Li, Si, and Zn, which were present below blank levels. The reproducibility of multiple analyses of a synthetic carbonate standard is presented in Table T7. In addition, six separate splits of interval 208-1264A-14H-5, 140–150 cm, were analyzed with the other samples, and the reproducibility of this consistency standard is given in Table T7. The Ca^{2+} content of the leachate was intended to be used for calculating CaCO_3 content by assuming that all Ca^{2+} was derived from CaCO_3 . However, the resulting Ca concentrations for all samples vary between $\sim 48\%$ and 53% Ca, indicating excess Ca was leached from a source other than the carbonate fraction (CaCO_3 consists of only 40% Ca). Therefore, the data cannot be used to calculate CaCO_3 content and results should be viewed as representing the carbonate plus other fractions with respect to the other elements analyzed.

T7. Reproducibility of sediment dissolution ICP-AES analyses results, p. 61.

Sediment Carbonate Analysis

The weight percentage of inorganic carbon (IC) in bulk sediment samples was determined using a Coulometrics 5011 CO_2 coulometer equipped with a System 140 carbonate analyzer. A total of ~ 10 – 12 mg of freeze-dried, ground sediment was reacted with 2-N HCl to liberate CO_2 . The change in light transmittance monitored by a photodetection cell controlled the CO_2 titration. The percentage of carbonate was calculated from the IC content using the following equation:

$$\text{CaCO}_3 \text{ (wt\%)} = \text{IC (wt\%)} \times 8.33.$$

This method assumes that all of the CO_2 evolved was derived from dissolution of calcium carbonate. No corrections were made for other carbonate minerals.

Sediment Organic Carbon Analysis

Total carbon (TC) content was determined using a Carlo Erba 1500 CHNS analyzer, which combusts sediment samples in tin cups with an

oxidant (V_2O_5) at 1000°C in a stream of oxygen. Nitrogen oxides were reduced to N_2 ; the mixture of N_2 , CO_2 , H_2O , and SO_2 gases was separated by gas chromatography; and detection was performed by a thermal conductivity detector. The H_2 value is not useful because it represents hydrogen derived from organic matter as well as water bound to clay minerals.

The analytical procedure employed a new combustion column for each sample batch. An aliquot of 5–15 mg of freeze-dried, crushed sediment with ~10 mg of V_2O_5 oxidant was combusted for each sample. All measurements were calibrated by comparison to a pure sulfanilamide standard. The amount of total organic carbon (TOC) was calculated as the difference between TC and IC (determined from coulometry) using the following equation:

$$\text{TOC (wt\%)} = \text{TC (wt\%)} - \text{IC (wt\%)}$$

Sediment Solvent-Extractable Components and Gas Chromatography–Mass Selective Detector

Solvent-extractable organic constituents were examined from selected samples to assess the characteristics of the organic matter present. The focus of these analyses was to qualitatively characterize organic matter, identify hydrocarbons and other components present, and determine their relative abundance. No quantitative determination of the concentrations of individual constituents was made.

Extraction procedures were as follows: ~10–50 g of sediment was extracted ultrasonically using CH_2Cl_2 (~80–100 mL) for 1 hr. A 12-hr extraction was performed on samples from some sites for characterization of heavier compounds. The extract was reduced to dryness under N_2 and then transferred in hexane to a column packed with 0.9–1.4 g of silica gel (deactivated with 5% of nanopure water) in a disposable pipette to remove polar constituents and recover hydrocarbon and ketone fractions by successive elution with hexane (2.5 mL) and CH_2Cl_2 (4 mL). Each eluate was taken to near dryness under N_2 and transferred in hexane (20–50 μL) to a vial (with small-volume insert) for analysis by gas chromatography with a mass selective detector (GC-MSD). The hexane eluate predominantly contains aliphatic hydrocarbons, and the CH_2Cl_2 eluate contains aromatic hydrocarbons and ketones.

An HP 5973 GC-MSD system consisting of an HP 6890 GC with an MSD and an HP 7683 automatic liquid sampler generated mass chromatograms, a total ion chromatogram for each eluate, and mass spectra for compounds detected. The GC is equipped with an EPC system, a split-splitless injector, and an HP capillary column (5% phenylmethylsiloxane; 30 m \times 0.25 μm ; HP-5) programmed from 70° to 130°C at $20^\circ\text{C}/\text{min}$, then at $4^\circ\text{C}/\text{min}$ to 320°C , and held isothermally at 320°C for 10 min. Helium is used as the carrier gas. The transfer line is set at 280°C , and the source of the MSD is set at 230°C . The MSD scanned from m/z (mass to charge ratio) 28 to 700. The HP MS Chemstation software was used for data acquisition and processing. The identity of individual hydrocarbons was determined from mass spectral characteristics and GC retention times by comparison with the literature.

DOWNHOLE MEASUREMENTS

Downhole logging tools are used to determine physical, chemical, and structural properties of the formation penetrated by drilling. Data are rapidly collected, continuous with depth, and, most importantly, measured in situ. Logs may be interpreted in terms of the stratigraphy, lithology, mineralogy, and geochemical composition of the penetrated formation. Where core recovery is good, logging and core data are complementary and should be integrated and interpreted jointly, with logging data providing in situ ground truth for core data. Where core recovery is incomplete or disturbed, logging data may provide the only means to characterize the borehole section.

Downhole logs record formation properties on a scale that is intermediate between those obtained from laboratory measurements on core samples and geophysical surveys. They are critical for calibrating geophysical survey data (e.g., through synthetic seismograms), providing the necessary link for the integration of core depth domain to seismic time domain data. Through logs, data collected at the borehole scale can be extended to a regional scale using geophysical surveys. Wireline logging was scheduled for three of the six sites cored during Leg 208.

Wireline Logging

Data are obtained by a variety of Schlumberger and LDEO logging tools, combined into several tool strings, which are deployed after coring operations in a hole are completed. The tool strings are deployed by lowering them to the bottom of the hole and recording data as they are pulled (at a constant rate) up the hole. Repeat runs, or short runs over critical intervals, are undertaken for data quality control. Three tool strings were run during Leg 208, although not all were run at every site. Details are given in individual site chapters. The three tool strings are

1. The triple combination (triple combo) tool string, consisting of resistivity (phasor Dual Induction Tool [DIT]), bulk density (Hostile Environment Litho-Density Sonde [HLDS]), gamma radiation (Hostile Environment Natural Gamma Ray Sonde [HNGS]), and porosity (Accelerator Porosity Sonde [APS]) components with two additional LDEO tools that measure high-resolution gamma radiation (Multi-Sensor Gamma Ray Tool [MGT]) and high-resolution temperature, acceleration, and pressure (Temperature/Acceleration/Pressure [TAP] tool).
2. The Formation MicroScanner (FMS)-sonic tool string, consisting of microresistivity (FMS), sonic velocity (Dipole Sonic Imager [DSI]), gamma radiation (Scintillation Gamma Ray Tool [SGT]), and orientation/acceleration (General Purpose Inclinerometer Tool [GPIT]) components.
3. The three-component Well Seismic Tool (WST-3), consisting of three geophones, pressed against the borehole wall, that are used to record the acoustic waves generated by an air gun located near the sea surface and offset from the ship.

NGR tools are included on both the triple combo and FMS-sonic tool strings to provide a common reference for correlation and depth shifting between multiple logging runs. WST-3 depths are taken from the wire-

ometer channel to improve data stacking by the precise measurement of logging speed. Postcruise processing may correct for borehole size and tool sticking by using the acceleration data.

Density

Formation density was determined with the HLDS. The tool contains a radioactive cesium (^{137}Cs) gamma ray source (622 keV) and far and near gamma ray detectors mounted on a shielded skid, which is pressed against the borehole wall. Gamma radiation emitted by the source undergoes Compton scattering, which involves the transfer of energy from gamma radiation to the electrons in the formation by way of elastic collisions. The amount of scattered gamma radiation that reaches the detectors is directly related to the density of electrons in the formation that is in turn related to bulk density. Porosity may also be derived from this bulk density if the matrix (grain) density is known. The HLDS also measures photoelectric absorption as the photoelectric effect (PEF). Photoelectric absorption of gamma radiation occurs when it reaches <150 keV after being repeatedly scattered by electrons in the formation. As the PEF depends on the atomic number of the elements in the formation, it also varies according to the chemical composition of the minerals present (Gardner and Dumanoir, 1980). For example, the PEF of calcite = 5.08 b/e⁻, illite = 3.03 b/e⁻, quartz = 1.81 b/e⁻, and kaolinite = 1.49 b/e⁻. Good contact between the tool and borehole wall is essential for the acquisition of quality HLDS logs; poor contact results in an underestimation of density values.

Porosity

Formation porosity was measured with the APS. The sonde incorporates a minitron neutron generator (which produces fast neutrons [14.4 MeV]) and five neutron detectors (four epithermal and one thermal) positioned at differing intervals from the minitron. The measurement principle involves counting neutrons that arrive at the detectors after being slowed by neutron absorbers surrounding the tool. The highest energy loss occurs when neutrons collide with hydrogen nuclei that have practically the same mass as the neutron (the neutrons simply bounce off heavier elements without losing much energy). If the hydrogen (i.e., water) concentration is small, as in low-porosity formations, neutrons can travel farther before being captured and the count rates increase at the detector. The opposite effect occurs when the water content is high. Because hydrogen bound in minerals such as clays or in hydrocarbons also contributes to the measurement, the raw porosity value is often overestimated. Upon reaching thermal energies of 0.025 eV, the neutrons are captured by the nuclei of Cl, Si, B, and other elements, resulting in a gamma ray emission. This neutron capture cross section (Σf) is also measured by the tool.

Electrical Resistivity

The DIT was used to measure electrical resistivity. The DIT provides three measures of electrical resistivity, each with a different depth of investigation into the formation. The two induction devices (deep and medium depths of penetration) transmit high-frequency alternating currents through transmitter coils, creating magnetic fields that induce secondary currents in the formation. These currents produce a new in-

ductive signal, proportional to the conductivity of the formation, which is measured by the receiving coils. The measured conductivities are then converted to resistivity. For the shallow-penetration resistivity, the current necessary to maintain a constant voltage drop across a fixed interval is measured; it is a direct measurement of resistivity. Sand grains and hydrocarbons are electrical insulators, whereas ionic solutions and clays are conductors. Electrical resistivity can therefore be used to evaluate porosity (using Archie's law) and fluid salinity.

Temperature, Acceleration, and Pressure

Downhole temperature, acceleration, and pressure were measured with the TAP tool. It was attached to the bottom of the triple combo tool string and run in memory mode with the data stored in the built-in memory. After the logging run was complete, the TAP tool was removed from the Schlumberger tools and returned to the DHML, where the data were downloaded.

The tool has a dual-temperature measurement system for identification of both rapid temperature fluctuations and temperature gradients. A thin fast-response thermistor detects small, abrupt changes in temperature, and the thicker slow-response thermistor more accurately estimates temperature gradients and thermal regimes. A pressure transducer is used to activate the tool at a specified depth, typically 200 m above the seafloor. A three-axis accelerometer measures tool movement downhole, which provides data for analyzing the effects of heave on the tool string. The long-term accumulation and analysis of these data, under varying cable lengths and heave conditions, will lead to enhanced performance of the WHC. Also, the acceleration log can aid in deconvolving heave effects postcruise, and it has proven at times to provide critical data. The temperature record must be interpreted with caution because the elapsed time between the end of drilling and the logging operation is generally not sufficient to allow the borehole to reach thermal equilibrium following circulation of the drilling fluid. The data recorded under such circumstances may differ significantly from the thermal equilibrium of that environment. Nevertheless, it is possible to identify abrupt temperature changes that may represent localized fluid flow into the borehole indicative of fluid pathways and fracturing and/or breaks in the temperature gradient that may correspond to contrasts in permeability at lithologic boundaries.

Acoustic Velocity

The DSI measures the transit times between sonic transmitters and an array of eight receivers. It averages replicate measurements, thus providing a direct measurement of sound velocity through sediments that is relatively free from the effects of formation damage and borehole enlargement (Schlumberger, 1989). The tool contains the monopole transmitters found on most sonic tools but also has two crossed dipole transmitters, providing shear wave velocity measurement in addition to the *P*-wave velocity, even in the slow formations typically encountered on paleoceanographic sediment legs.

Formation MicroScanner

The FMS-sonic tool string provides high-resolution electrical resistivity-derived images of the borehole wall. The tool has four orthogonal

arms with pads, each containing 16 button electrodes that are pressed against the borehole wall during the recording (Fig. F6). The electrodes are arranged in two diagonally offset rows of 8 electrodes. A focused current is emitted from the button electrodes into the formation, with a return electrode located near the top of the tool. The intensity of current passing through the button electrodes is measured. Processing transforms these measurements, which reflect the microresistivity variations of the formation, into continuous, spatially oriented, high-resolution images that map the geologic structures of the borehole wall. Analysis of the processed FMS images can provide measurements of dip and direction (azimuth) of structural features in the formation.

The development of the FMS-sonic tool string has added a new dimension to wireline logging (Luthi, 1990; Lovell et al., 1998). Features such as bedding, fracturing, slump folding, and bioturbation can be resolved, and spatially oriented images allow fabric analysis and bed orientations to be measured. The maximum extension of the caliper arms is 15 in, so in holes or parts of holes with a larger diameter, the pad contact will be inconsistent and the FMS images may appear out of focus and too conductive. Irregular borehole walls will also adversely affect the image quality if they lead to poor pad-wall contact. Acceleration and magnetic field measurements were made with the GPIT. The primary purpose of this tool, which incorporates a three-component accelerometer and a three-component magnetometer, is to determine the acceleration and orientation of the FMS-sonic tool string during logging. This provides a means of correcting the FMS images for irregular tool motion and allows the true dip and direction (azimuth) of structures to be determined.

Logging Data Quality

The principal influence on logging data quality is the condition of the borehole wall. If the borehole diameter is variable over short intervals, resulting from washouts during drilling, clay swelling, or ledges caused by layers of harder material, the logs from those tools that require good contact with the borehole wall (i.e., FMS, density, and porosity tools) may be degraded. Deep investigation measurements such as resistivity and sonic velocity, which do not require contact with the borehole wall, are generally less sensitive to borehole conditions. Very narrow ("bridged") sections will also cause irregular logging results. The quality of the borehole is improved by minimizing the circulation of drilling fluid while drilling, flushing the borehole to remove debris, and logging as soon as possible after drilling and hole conditioning are completed. These procedures were followed in all logging operations during Leg 208.

Logging Depth Scales

The depth of the wireline-logged measurement is determined from the length of the logging cable extended from the winch on the ship. When possible, the seafloor is identified on the NGR log by the abrupt reduction in gamma ray count at the water/sediment boundary (mudline). The coring depth (drillers depth) is determined from the known length of the BHA and pipe stands. The mudline is usually recovered in the first core from the hole.

Discrepancies between the drillers depth of recovered core and the wireline logging depth occur because of core expansion, incomplete

core recovery, incomplete heave compensation, drill pipe stretch in the case of drill pipe depth, cable stretch (~1 m/km), and cable slip in the case of logging depth. Tidal changes in sea level will also have an effect. To minimize the wireline tool motion caused by ship heave, the WHC adjusts for rig motion during wireline logging operations. The small but significant differences between drill pipe depth and logging depth should be taken into account when using the logs for correlation between core and logging data. The depths of core data sets, such as density and natural gamma radiation, can be correlated with the equivalent downhole logs using programs such as Sagan, which allow mapping of the core depths onto the logging depth scale. In zones where core recovery is low, precise core-log depth matching may be difficult because of the inherent ambiguity of placing the recovered section within the cored interval. Where complete core recovery (using a composite depth splice) (Hagelberg et al., 1992) is achieved, core depths and densities can be corrected by correlation with the logging data.

Logs from different wireline tool strings will have slight depth mismatches. Distinctive features recorded by the natural gamma tools (Fig. F6) run on every tool string (except the WST-3) provide relative depth offsets and a means of depth shifting for correlation between logging runs.

Data Recording and Processing

Data for each logging run were recorded, stored digitally, and monitored in real time using the MCM software. On completion of logging in each hole, data acquisition processing by the Schlumberger engineer is completed; data were subsequently transferred to the DHML and transmitted via satellite to LDEO-BRG for shore-based processing. Data processing at LDEO-BRG consists of (1) depth shifting all logs relative to a common datum (i.e., mbsf), (2) corrections specific to individual tools, and (3) quality control and rejection of unrealistic or spurious values. Once processed at LDEO-BRG, logging data were transmitted back to the ship, providing near-real time data processing.

As a further check of data quality and log interpretation, wavelet analysis of the tool strings' accelerometer data and other standard logs may be undertaken. Continuous wavelet analysis allows rapid localization of cyclic patterns or discontinuities, both in space (depth) and scale (e.g., Torrence and Compo, 1998). In contrast to classical Fourier transform or windowed Fourier transform that decompose the original signal on the basis of an infinite periodic function depending on a unique parameter (space frequency), the wavelet transform allows a "depth-scale" representation that depends on a scale parameter and a translation parameter. The scale parameter (or dilatation factor) determines the characteristic frequencies at which the wavelet transform is computed, and the translation parameter allows local analysis. A reading of the wavelet power spectrum can be obtained by constructing a color diagram with the depth on the vertical axis and the scales (or the equivalent Fourier periods) on the horizontal axis, the modulus of the wavelet transform being represented by colored patches. This type of diagram is therefore comparable to an evolutionary power spectrum and can be revealing about the structure of a particular process. The main difference between the wavelet and the Fourier decomposition is in the support of the respective basis functions. The wavelet transform coefficients are influenced by local events, whereas the Fourier coefficients are influenced by the function on its entire domain. This makes

the wavelet spectrum a better measure of the variance attributed to localized events. To facilitate the interpretation of this type of diagram, one can define a level above which a maximum in the wavelet spectrum is statistically significant. It has been shown that each point in the wavelet power spectrum has a c^2 distribution with 2 degrees of freedom about the background spectrum (Torrence and Compo, 1998). The confidence level at each scale is therefore the product of the background spectrum and the desired significance level (for instance 95% confidence) from the c^2 distribution. Here, the background spectrum is determined by calculating the depth average of the wavelet spectrum.

Further postcruise processing of the logging data from the FMS-sonic tool string is performed at LDEO-BRG. Postcruise-processed logging data are available directly from the LDEO-BRG World Wide Web site at www.ldeo.columbia.edu/BRG/ODP/DATABASE/. A summary of “logging highlights” is posted on the LDEO-BRG Web site at the end of each leg. Basic processing was conducted postcruise to provide scientists with a comprehensive, quality-controlled downhole logging data set that can be used for comparison, integration, and correlation with other data collected during Leg 208 and other ODP legs. The processing includes depth adjustments to remove depth offsets between data from different logging runs, corrections specific to certain tools and logs, documentation for the logs (with an assessment of log quality), and conversion of the data to a widely accessible format (ASCII). Schlumberger GeoQuest’s GeoFrame software package is used for most of the processing. Processed ASCII files of acoustic, caliper, density, gamma ray, magnetic, neutron porosity, resistivity, and temperature data are available, with FMS images as GIF files.

AGE MODEL AND MASS ACCUMULATION RATES

Biostratigraphic, paleomagnetic, and other data, if available, were used to construct age-depth models for all Leg 208 sites. The models are tabulated in the site chapters and plotted with all reliable age control points from which the models were derived. The depths used were mcd for each site (see “[Composite Depth](#),” p. 4). For the “[Leg 208 Summary](#)” chapter age plots, ~300 cyclostratigraphic tie points derived from the MST data were used to align the individual sites and thereby increase the precision of the age-depth models.

Linear sedimentation rates (LSRs) were calculated for 1-m.y. time intervals, and corrected LSRs were computed to compensate for the growth rates inherent in the mcd scale. Dry density data were used to convert corrected LSRs to total mass accumulation rates (MARs). Carbonate concentration data were used to estimate carbonate MARs. The results are briefly discussed in the site chapters and in the “[Leg 208 Summary](#)” chapter. The following is a description of the modeling principles employed and computations performed.

Age-Depth Model

The timescales applied to the Leg 208 biostratigraphic and paleomagnetic datums are (1) the astronomically tuned timescale for the Neogene by Lourens et al. (in press) and H. Pälike et al. (pers. comm., 2003) for the late early–late Oligocene and (2) the geomagnetic polarity time-

scale of Cande and Kent (1995) for the Late Cretaceous to early Oligocene (top Chron C12n) time interval. Construction of the astronomically tuned timescale was based on tuning sedimentary successions from the western equatorial Atlantic Ocean (Ceara Rise, Leg 154), Mediterranean, and equatorial Pacific (Leg 199) (Lourens et al., in press) to the La2003 (Laskar et al., unpubl. data) full numerical solution. A sea-floor anomaly profile from the Antarctic-Australian plate pair was employed to complete the polarity timescale for the interval between 13 and 23 Ma because of the lack of magnetostratigraphic records for ODP Leg 154 sites. The astronomical timescale resulted in a significantly younger age of 23.03 Ma for the O/M boundary than the 23.8 Ma age preferred in previous timescales (Berggren et al., 1995b).

The biohorizons used for Leg 208 are either directly tied to the new timescale via first-order calibrations, such as the standard low-latitude calcareous plankton zonations, or can be linked to it by recalibrating them to the associated polarity timescale. The ages for the biostratigraphic and magnetostratigraphic tie points are tabulated in “**Magnetostratigraphy**,” p. 22, in “Paleomagnetism” and in “**Biostratigraphy**,” p. 14.

The precision of the shipboard Leg 208 site-specific age-depth models is limited because of the generally low biostratigraphic sampling resolution (1.5–10 m) and the varying quality of the paleomagnetic results. We applied a procedure that resulted in conservative shipboard age models, satisfying as many constraints as possible without introducing artificial or speculative features. Construction of the age-depth curve for each site started with a plot of all control points from biostratigraphy and paleomagnetism. Age and depth uncertainties were represented by error bars. Obvious outliers and conflicting datums were then masked until the line connecting the remaining control points was contiguous (i.e., without age-depth inversions). Next, an interpolation curve was applied that passed through all control points with smooth inflections. Some tie points were depth shifted within their range of uncertainty to minimize the change of slope at the inflection points and to yield the smoothest age-depth curve possible.

Paleomagnetic data, if available and reasonably well calibrated with biostratigraphic data, were usually given first priority in constraining the age-depth model in case of conflicting datums, followed by calcareous nannofossils and planktonic foraminifers. In cases of conflicting microfossil datums, we also took into account the reliability of individual datums as global dating tools, the stratigraphic reliability of fossil groups or specific datums, abundance, preservation, and reworking, if indicated, and the uncertainties associated with the first or last occurrence of a datum (first occurrence datums are generally preferred).

In each site chapter, the age models are presented as plots of original datums with error bars overlain by the smooth age model and tabulated as age-depth series. For the age plots in Table T2, p. 107, in the “**Leg 208 Summary**” chapter, ~300 cyclostratigraphic tie points derived from the MST data were used to align the individual sites and thereby increase the precision of the age model.

Linear Sedimentation Rates and Mass Accumulation Rates

Once the final age models were defined, calculating and plotting LSRs and MARs was a process that involved a number of simple interpolations and computations. The only subjective part in that process was

the selection of time intervals at which the smooth age model was sampled. Instead of calculating LSRs and MARs over intervals given by the original stratigraphic control points, we decided to choose regular and conservative time intervals. As a rule of thumb, a time interval should include at least three age control points (on average). It should be kept in mind that the time series is an arbitrary choice of an average sampling rate and does not reflect the resolution of the age model equally in all intervals. However, in conjunction with a smooth age model, it presents a realistic and conservative trend in LSRs and MARs.

First, we sampled the site-specific age models at 1-m.y. intervals to obtain interpolated depths in mcd for those ages. LSRs in meters per million years were then calculated as the first derivative of the age-depth series over the selected interval. The LSRs were subsequently corrected for the expansion of the recovered sediment sequence, as represented by the ratio of the mcd scale vs. the mbsf scale (see **“Composite Depth,”** p. 4), dividing the LSR by the appropriate growth factor for each depth interval.

In preparation for computing the MARs, dry density obtained from MAD measurements (see **“Physical Properties,”** p. 11) and carbonate concentration data (see **“Geochemistry,”** p. 23) were plotted against mcd and outliers were removed. Ages were interpolated for each depth point using the age-depth model. Dry density and carbonate records were averaged over the regular 1-m.y. time intervals. This averaging step is important to avoid a commonly introduced bias that occurs when dry density data at relatively high age/depth resolution are multiplied by LSRs calculated at a much lower resolution. Such a bias gives the impression that we know the MAR variations at a high age/time and amplitude resolution, when, in fact, associated LSR variations overwhelm those trends and may also directly compensate for the dry density variations (higher dry density typically results in lower LSR). The generally low resolution of LSRs determines the resolution of MAR variations, even if the available dry density (or carbonate) record has a much higher resolution.

MARs were calculated using the equation:

$$\text{bulk MAR (g/cm}^2\text{/k.y.)} = \text{LSR (m/m.y.)} \times \text{dry density (g/cm}^3\text{)}/10.$$

Carbonate MARs were calculated by multiplying the bulk MAR by the fractional concentration of calcium carbonate.

Finally, a step plot of LSR, total MAR, and carbonate MAR summarizes the data in each site chapter. Although a smooth plot through the midpoints of the age intervals would convey the same information, we prefer the step plot because it illustrates clearly the selected age resolution that we consider to be reasonable and conservative.

REFERENCES

- Alegret, L., and Thomas, E., 2001. Upper Cretaceous and lower Paleogene benthic foraminifera from northeastern Mexico. *Micropaleontology*, 47:269–316.
- Aubry, M.-P., Berggren, W.A., Stott, L., and Sinha, A., 1996. The upper Paleocene–lower Eocene stratigraphic record and the Paleocene/Eocene boundary carbon isotope excursion: implications for geochronology. In Knox, R.W.O'B., Corfield, R.M., and Dunay, R.E. (Eds.), *Correlation of the Early Paleogene in Northwestern Europe*. Geol. Soc. Spec. Publ., 101:353–380.
- Backman, J., 1986. Late Paleocene to middle Eocene calcareous nannofossil biochronology from the Shatsky Rise, Walvis Ridge and Italy. *Palaeogeogr., Palaeoclimatol., Palaeoecol.*, 57:43–59.
- , 1987. Quantitative calcareous nannofossil biochronology of middle Eocene through early Oligocene sediment from DSDP Sites 522 and 523. *Abh. Geol. Bundesanst. (Austria)*, 39:21–31.
- Backman, J., and Raffi, I., 1997. Calibration of Miocene nannofossil events to orbitally tuned cyclostratigraphies from Ceara Rise. In Shackleton, N.J., Curry, W.B., Richter, C., and Bralower, T.J. (Eds.), *Proc. ODP, Sci. Results*, 154: College Station, TX (Ocean Drilling Program), 83–99.
- Balsam, W.L., Damuth, J.E., and Schneider, R.R., 1997. Comparison of shipboard vs. shore-based spectral data from Amazon-Fan cores: implications for interpreting sediment composition. In Flood, R.D., Piper, D.J.W., Klaus, A., and Peterson, L.C. (Eds.), *Proc. ODP, Sci. Results*, 155: College Station, TX (Ocean Drilling Program), 193–215.
- Balsam, W.L., Deaton, B.C., and Damuth, J.E., 1998. The effects of water content on diffuse reflectance measurements of deep-sea core samples: an example from ODP Leg 164 sediments. *Mar. Geol.*, 149:177–189.
- , 1999. Evaluating optical lightness as a proxy for carbonate content in marine sediment cores. *Mar. Geol.*, 161:141–153.
- Berggren, W.A., Hilgen, F.J., Langereis, C.G., Kent, D.V., Obradovich, J.D., Raffi, I., Raymo, M.E., and Shackleton, N.J., 1995a. Late Neogene chronology: new perspectives in high-resolution stratigraphy. *Geol. Soc. Am. Bull.*, 107:1272–1287.
- Berggren, W.A., Kent, D.V., Swisher, C.C., III, and Aubry, M.-P., 1995b. A revised Cenozoic geochronology and chronostratigraphy. In Berggren, W.A., Kent, D.V., Aubry, M.-P., and Hardenbol, J. (Eds.), *Geochronology, Time Scales and Global Stratigraphic Correlation*. Spec. Publ.—SEPM (Soc. Sediment. Geol.), 54:129–212.
- Blum, P., 1997. Physical properties handbook: a guide to the shipboard measurement of physical properties of deep-sea cores. *ODP Tech. Note*, 26 [Online]. Available from World Wide Web: <<http://www-odp.tamu.edu/publications/tnotes/tn26/INDEX.HTM>>. [Cited 2003-03-06]
- Bolli, H.M., and Saunders, J.B., 1985. Oligocene to Holocene low latitude planktic foraminifera. In Bolli, H.M., Saunders, J.B., and Perch-Nielsen, K. (Eds.), *Plankton Stratigraphy*: Cambridge (Cambridge Univ. Press), 155–262.
- Boltovskoy, E., 1978. Late Cenozoic benthonic Foraminifera of the Ninetyeast Ridge (Indian Ocean). *Mar. Geol.*, 26:139–178.
- Boltovskoy, E., and Boltovskoy, D., 1989. Paleocene–Pleistocene benthic foraminifer evidence of major paleoceanographic events in the eastern South Atlantic (DSDP Site 525, Walvis Ridge). *Mar. Micropaleontol.*, 14:283–316.
- Boltovskoy, E., and Watanabe, S., 1993. Cenozoic monothalamous foraminifers from DSDP Site 525 (southern Atlantic). *Micropaleontology*, 39:1–27.
- Boltovskoy, E., Watanabe, S., Totah, V., and Ocampo, J.V., 1995. Benthic foraminifers from DSDP Site 516 (upper Maestrichtian–Quaternary, South Atlantic). *Rev. Esp. Micropaleontol.*, 27:111–139.
- Bown, P.R. (Ed.), 1999. *Calcareous Nannofossil Biostratigraphy*: Dordrecht, Netherlands (Kluwer Academic Publishers).

- Bralower, T.J., Leckie, R.M., Sliter, W.V., and Thierstein, H.R., 1995. An integrated Cretaceous microfossil biostratigraphy. *In* Berggren, W.A., Kent, D.V., Aubry, M.-P., and Hardenbol, J. (Eds.), *Geochronology, Time Scales, and Global Stratigraphic Correlation*. Spec. Publ.—SEPM (Soc. Sediment. Geol.), 54:65–79.
- Bralower, T.J., and Mutterlose, J., 1995. Calcareous nannofossil biostratigraphy of Site 865, Allison Guyot, Central Pacific Ocean: a tropical Paleogene reference section. *In* Winterer, E.L., Sager, W.W., Firth, J.V., and Sinton, J.M. (Eds.), *Proc. ODP, Sci. Results*, 143: College Station, TX (Ocean Drilling Program), 31–74.
- Bukry, D., 1973. Low-latitude coccolith biostratigraphic zonation. *In* Edgar, N.T., Saunders, J.B., et al., *Init. Repts. DSDP*, 15: Washington (U.S. Govt. Printing Office), 685–703.
- , 1975. Coccolith and silicoflagellate stratigraphy, northwestern Pacific Ocean, Deep Sea Drilling Project Leg 32. *In* Larson, R.L., Moberly, R., et al., *Init. Repts. DSDP*, 32: Washington (U.S. Govt. Printing Office), 677–701.
- , 1991. Paleoecological transect of western Pacific Ocean late Pliocene coccolith flora, Part I. Tropical Ontong-Java Plateau at ODP 806B. *Open-File Rep.—U.S. Geol. Surv.*, 91-552:1–35.
- Burton, J.D., 1996. The ocean: a global geochemical system. *In* Summerhayes, C.P., and Thorpe, S.A. (Eds.), *Oceanography: An Illustrated Guide*: London (Manson Publishing Ltd.), 166.
- Cande, S.C., and Kent, D.V., 1995. Revised calibration of the geomagnetic polarity timescale for the Late Cretaceous and Cenozoic. *J. Geophys. Res.*, 100:6093–6095.
- Caron, M., 1985. Cretaceous planktic foraminifera. *In* Bolli, H.M., Saunders, J.B., and Perch-Nielsen, K. (Eds.), *Plankton Stratigraphy*: Cambridge (Cambridge Univ. Press), 17–86.
- Chaisson, W.P., and Leckie, R.M., 1993. High-resolution Neogene planktonic foraminifer biostratigraphy of Site 806, Ontong Java Plateau (western equatorial Pacific). *In* Berger, W.H., Kroenke, L.W., Mayer, L.A., et al., *Proc. ODP, Sci. Results*, 130: College Station, TX (Ocean Drilling Program), 137–178.
- Chaisson, W.P., and Pearson, P.N., 1997. Planktonic foraminifer biostratigraphy at Site 925: middle Miocene–Pleistocene. *In* Shackleton, N.J., Curry, W.B., Richter, C., and Bralower, T.J. (Eds.), *Proc. ODP, Sci. Results*, 154: College Station, TX (Ocean Drilling Program), 3–31.
- Coccioni, R., Monaco, P., Monechi, S., Nocchi, M., and Parisi, G., 1988. Biostratigraphy of the Eocene–Oligocene boundary at Massignano (Ancona, Italy). *In* Premoli Silva, I., Coccioni, R., and Montanari, A. (Eds.), *The Eocene-Oligocene Boundary in the Marche-Umbria Basin (Italy)*: Ancona (Int. Union Geol. Sci.), 59–80.
- Culver, S.J., 2003. Benthic foraminifera across the Cretaceous–Tertiary (K–T) boundary: a review. *Mar. Micropaleontol.*, 14:177–226.
- Ellis, D.V., 1987. *Well Logging for Earth Scientists*: New York (Elsevier).
- Erba, E., Premoli Silva, I., and Watkins, D.K., 1995. Cretaceous calcareous plankton biostratigraphy of Sites 872 through 879. *In* Haggerty, J.A., Premoli Silva, I., Rack, F., and McNutt, M.K. (Eds.), *Proc. ODP, Sci. Results*, 144: College Station, TX (Ocean Drilling Program), 157–169.
- Fuller, M., Hastedt, M., and Herr, B., 1998. Coring-induced magnetization of recovered sediment. *In* Weaver, P.P.E., Schmincke, H.-U., Firth, J.V., and Duffield, W. (Eds.), *Proc. ODP, Sci. Results*, 157: College Station, TX (Ocean Drilling Program), 47–56.
- Galeotti, S., Kaminski, M.A., Coccioni, R., and Speijer, R., in press. High resolution deep water agglutinated foraminiferal record across the Paleocene/Eocene transition in the Contessa Road Section (Italy). *In* Hart, M.B., Kaminski, M.A., and Smart, C. (Eds.), *Proc. 6th Int. Workshop Agglutinated Foraminifera*.
- Gardener, J.S., and Dumanoir, J.L., 1980. Litho-density log interpretation. *Trans. SPWLA Annu. Logging Symp.*, 21:1–23.

- Gieskes, J.M., Johnston, K., and Boehm, M., 1984. Interstitial water studies, Leg 74. In Moore, T.C., Rabinowitz, P.D., et al., *Init. Repts., DSDP, 74*: Washington (U.S. Govt. Printing Office), 701–711.
- Goldberg, D., 1990. Test performance of the Ocean Drilling Program wireline heave motion compensator. *Sci. Drill.*, 1:206–209.
- , 1997. The role of downhole measurements in marine geology and geophysics. *Rev. Geophys.*, 35:315–342.
- Hagelberg, T., Shackleton, N., Pisias, N., and Shipboard Scientific Party, 1992. Development of composite depth sections for Sites 844 through 854. In Mayer, L., Pisias, N., Janecek, T., et al., *Proc. ODP, Init. Repts.*, 138 (Pt. 1): College Station, TX (Ocean Drilling Program), 79–85.
- Hayward, B.W., 2002. Late Pliocene to middle Pleistocene extinctions of deep-sea benthic foraminifera (“*Stilostomella* extinction”) in the southwest Pacific. *J. Foraminiferal Res.*, 32:274–307.
- Hemleben, C., Kaminski, M.A., Kuhnt, W., and Scott, D.B. (Eds.), 1990. *Proceedings of the NATO Advanced Study Institute on Paleocology, Biostratigraphy, Paleoceanography and Taxonomy of Agglutinated Foraminifera*. NATO ASI Ser., Ser. C, Vol. 327.
- Hilgen, F.J., 1991. Extension of the astronomically calibrated (polarity) time scale to the Miocene/Pliocene boundary. *Earth Planet. Sci. Lett.*, 107:349–368.
- Kaminski, M.A., Kuhnt, W., and Radley, J., 1996. Palaeocene–Eocene deep water agglutinated foraminifera from the Numidian Flysch (Rif, Northern Morocco): their significance for the palaeoceanography of the Gibraltar gateway. *J. Micropaleontol.*, 15:1–19.
- Kelly, D.C., 2002. Response of Antarctic (ODP Site 690) planktonic foraminifera to the Paleocene–Eocene Thermal Maximum: faunal evidence for ocean/climate change. *Paleoceanography*, 17:10.1029/2002PA000761.
- Kelly, D.C., Bralower, T.J., and Zachos, J.C., 1998. Evolutionary consequences of the latest Paleocene Thermal Maximum for tropical planktonic foraminifera. *Palaeogeogr., Palaeoclimatol., Palaeoecol.*, 141:139–161.
- Kelly, D.C., Bralower, T.J., Zachos, J.C., Premoli Silva, I., and Thomas, E., 1996. Rapid diversification of planktonic foraminifera in the tropical Pacific (ODP Site 865) during the late Paleocene Thermal Maximum. *Geology*, 24:423–426.
- Kennett, J.P., and Srinivasan, M.S., 1983. *Neogene Planktonic Foraminifera: A Phylogenetic Atlas*: Stroudsburg, PA (Hutchinson Ross).
- Loeblich, A.R., and Tappan, H., 1988. *Foraminiferal Genera and Their Classification* (Vol. 2): New York (Van Nostrand Reinhold Company).
- Lourens, L.J., Antonarakou, A., Hilgen, F.J., Van Hoof, A.A.M., Vergnaud-Grazzini, C., and Zachariasse, W.J., 1996. Evaluation of the Plio–Pleistocene astronomical time-scale. *Paleoceanography*, 11:391–413.
- Lourens, L.J., Hilgen, F.J., Laskar, J., Shackleton, N.J., and Wilson, D., in press. The Neogene period. In Gradstein, F.M., Ogg, J., and Smith, A.G. (Eds.), *A Geological Time Scale 2004*: Cambridge (Cambridge Univ. Press).
- Lovell, M.A., Harvey, P.K., Brewer, T.S., Williams, C., Jackson, P.D., and Williamson, G., 1998. Application of FMS images in the Ocean Drilling Program: an overview. In Cramp, A., MacLeod, C.J., Lee, S.V., and Jones, E.J.W. (Eds.), *Geological Evolution of Ocean Basins: Results from the Ocean Drilling Program*. Geol. Soc. Spec. Publ., 131:287–303.
- Luterbacher, H.P., Hardenbol, J., and Schmitz, B., 2000. Decision of the voting members of the International Subcommission on Paleogene Stratigraphy on the criterion for the recognition of the Paleocene/Eocene boundary. *Newsl. Int. Subcomm. Paleogene Stratigr.*, 9:13.
- Luthi, S.M., 1990. Sedimentary structures of clastic rocks identified from electrical borehole images. In Hurst, A., Lovell, M.A., and Morton, A.C. (Eds.), *Geological Applications of Wireline Logs*. Spec. Publ.—Geol. Soc. London, 48:3–10.

- Lyle, M.W., Wilson, P.A., Janecek, T.R., et al., 2002. *Proc. ODP, Init. Repts.*, 199 [CD-ROM]. Available from: Ocean Drilling Program, Texas A&M University, College Station TX 77845-9547, USA.
- Mackenzie, K.V., 1981. Nine-term equation for sound speed in the oceans. *J. Acoust. Soc. Am.*, 70:807–812.
- Manheim, F.T., and Sayles, F.L., 1974. Composition and origin of interstitial waters of marine sediments, based on deep sea drill cores. In Goldberg, E.D. (Ed.), *The Sea* (Vol. 5): *Marine Chemistry: The Sedimentary Cycle*: New York (Wiley), 527–568.
- Martini, E., 1971. Standard Tertiary and Quaternary calcareous nannoplankton zonation. In Farinacci, A. (Ed.), *Proc. 2nd Int. Conf. Planktonic Microfossils Roma*: Rome (Ed. Tecnosci.), 2:739–785.
- Monechi, S., and Thierstein, H.R., 1985. Late Cretaceous–Eocene nannofossil and magnetostratigraphic correlations near Gubbio, Italy. *Mar. Micropaleontol.*, 9:419–440.
- Müller-Merz, E., and Oberhänsli, H., 1991. Eocene bathyal and abyssal benthic foraminifera from a South Atlantic transect at 20–30°S. *Palaeogeogr., Palaeoclimatol., Palaeoecol.*, 83:117–171.
- Murray, R.W., Miller, D.J., and Kryc, K.A., 2000. Analysis of major and trace elements in rocks, sediments, and interstitial waters by inductively coupled plasma–atomic emission spectrometry (ICP–AES). *ODP Tech. Note, 29* [Online]. Available from World Wide Web: <<http://www-odp.tamu.edu/publications/tnotes/tn29/INDEX.HTM>>. [Cited 2003-03-06]
- Nomura, R., 1995. Paleogene to Neogene deep-sea paleoceanography in the eastern Indian Ocean: benthic foraminifera from ODP Sites 747, 757, and 758. *Micropaleontology*, 41:251–290.
- Norris, R.D., Huber, B.T., and Self-Trail, J., 1999. Synchronicity of the K-T oceanic mass extinction and meteorite impact: Blake Nose, western North Atlantic. *Geology*, 27:419–422.
- Norris, R.D., and Röhl, U., 1999. Carbon cycling and chronology of climate warming during the Palaeocene/Eocene transition. *Nature*, 401:775–778.
- Okada, H., and Bukry, D., 1980. Supplementary modification and introduction of code numbers to the low-latitude coccolith biostratigraphic zonation (Bukry, 1973; 1975). *Mar. Micropaleontol.*, 5:321–325.
- Olsson, R.K., Hemleben, C., Berggren, W.A., and Huber, B.T. (Eds.), 1999. *Atlas of Paleocene Planktonic Foraminifera*. Smithsonian Contrib. Paleobiol., Vol. 85.
- Parker, R.L., and Gee, J.S., 2002. Calibration of the pass-through magnetometer—II. Application. *Geophys. J. Int.*, 150:140–152.
- Pearson, P.N., and Chaisson, W.P., 1997. Late Paleocene to middle Miocene planktonic foraminifer biostratigraphy of the Ceara Rise. In Shackleton, N.J., Curry, W.B., Richter, C., and Bralower, T.J. (Eds.), *Proc. ODP, Sci. Results, 154*: College Station, TX (Ocean Drilling Program), 33–68.
- Perch-Nielsen, K., 1985. Cenozoic calcareous nannofossils. In Bolli, H.M., Saunders, J.B., and Perch-Nielsen, K. (Eds.), *Plankton Stratigraphy*: Cambridge (Cambridge Univ. Press), 427–554.
- Pimmel, A., and Claypool, G., 2001. Introduction to shipboard organic geochemistry on the *JOIDES Resolution*. *ODP Tech. Note, 30* [Online]. Available from World Wide Web: <<http://www-odp.tamu.edu/publications/tnotes/tn30/INDEX.HTM>>. [Cited 2003-03-06]
- Postuma, J.A., 1971. *Manual of Planktonic Foraminifera*: Amsterdam (Elsevier).
- Premoli Silva, I., and Sliter, W.V., 1999. Cretaceous paleoceanography: evidence from planktonic foraminiferal evolution. In Barrera, E., and Johnson, C.C. (Eds.), *The Evolution of Cretaceous Ocean-Climatic System*. Spec. Pap.—Geol. Soc. Am., 332:301–328.
- Raffi, I., 2002. Revision of the early–middle Pleistocene calcareous nannofossil biochronology (1.75–0.85 Ma). *Mar. Micropaleontol.*, 45:25–55.

- Raffi, I., Backman, J., Rio, D., and Shackleton, N.J., 1993. Plio–Pleistocene nannofossil biostratigraphy and calibration to oxygen isotopes stratigraphies from Deep Sea Drilling Project Site 607 and Ocean Drilling Program Site 677. *Paleoceanography*, 8:387–408.
- Raffi, I., and Flores, J.-A., 1995. Pleistocene through Miocene calcareous nannofossils from eastern equatorial Pacific Ocean. In Pisias, N.G., Mayer, L.A., Janecek, T.R., Palmer-Julson, A., and van Andel, T.H. (Eds.), *Proc. ODP, Sci. Results*, 138: College Station, TX (Ocean Drilling Program), 233–286.
- Rider, M.H., 1996. *The Geological Interpretation of Well Logs* (2nd ed.): Caithness (Whittles Publishing).
- Röhl, U., Bralower, T.J., Norris, R.D., and Wefer, G., 2000. New chronology for the late Paleocene thermal maximum and its environmental implications. *Geology*, 28:927–930.
- Röhl, U., Norris, R.D., and Ogg, J.G., 2003. Cyclostratigraphy of upper Paleocene and late Eocene sediments at Blake Nose Site 1051 (western North Atlantic). In Gingerich, P., Schmitz, B., and Thomas, E. (Eds.), *Causes and Consequences of Globally Warm Climates in the Early Paleogene*. Spec. Pap.—Geol. Soc. Am., 369:567–589.
- Roth, P.H., 1978. Cretaceous nannoplankton biostratigraphy and oceanography of the northwestern Atlantic Ocean. In Benson, W.E., Sheridan, R.E., et al., *Init. Repts. DSDP*, 44: Washington (U.S. Govt. Printing Office), 731–759.
- Ruddiman, W.F., Cameron, D., and Clement, B.M., 1987. Sediment disturbance and correlation of offset holes drilled with the hydraulic piston corer: Leg 94. In Ruddiman, W.F., Kidd, R.B., Thomas, E., et al., *Init. Repts. DSDP*, 94 (Pt. 2): Washington (U.S. Govt. Printing Office), 615–634.
- Schlumberger, 1989. *Log Interpretation Principles/Applications*: Houston (Schlumberger Educ. Services), SMP-7017.
- , 1994. *IPL Integrated Porosity Lithology*: Houston (Schlumberger Wireline and Testing), SMP-9270.
- Schmiedl, G., Mackensen, A., and Müller, P.J., 1997. Recent benthic foraminifera from the eastern South Atlantic Ocean: dependence on food supply and water masses. *Mar. Micropaleontol.*, 32:249–287.
- Serra, O., 1984. *Fundamentals of Well-Log Interpretation* (Vol. 1): *The Acquisition of Logging Data*. Dev. Pet. Sci., 15A.
- , 1986. *Fundamentals of Well-Log Interpretation* (Vol. 2): *The Interpretation of Logging Data*. Dev. Pet. Sci., 15B.
- , 1989. *Formation MicroScanner Image Interpretation*: Houston (Schlumberger Educ. Services), SMP-7028.
- Shackleton, N.J., Crowhurst, S.J., Weedon, G.P., and Laskar, J., 1999. Astronomical calibration of Oligocene–Miocene time. *Philos. Trans. R. Soc. London, Ser. A*, 357:1907–1929.
- Shackleton, N.J., Raffi, I., and Röhl, U., 2001. Astronomical age calibration in the middle Miocene. *Eos, Trans. Am. Geophys. Union*, 32 (Suppl.): 31.
- Sissingh, W., 1977. Biostratigraphy of Cretaceous calcareous nannoplankton. *Geol. Mijnbouw*, 56:37–65.
- Speijer, R.P., and Samir, A.M., 1997. *Globanomalina luxorensis*, a Tethyan biostratigraphic marker of latest Paleocene global events. *Micropaleontology*, 43:49–60.
- Spezzaferri, S., 1994. Planktonic foraminiferal biostratigraphy and taxonomy of the Oligocene and lower Miocene in the oceanic record: an overview. *Palaeontographica Ital.*, 81:1–187.
- Spezzaferri, S., and Premoli Silva, I., 1991. Oligocene planktonic foraminiferal biostratigraphy and paleoclimatic interpretation from Hole 538A, DSDP Leg 77, Gulf of Mexico. *Palaeogeogr., Palaeoclimatol., Palaeoecol.*, 83:217–263.
- Thierstein, H.R., Geitzenauer, K., Molino, B., and Shackleton, N.J., 1977. Global synchronicity of late Quaternary coccolith datum levels: validation by oxygen isotopes. *Geology*, 5:400–404.

- Thomas, E., 1985. Late Eocene to Recent deep-sea benthic foraminifers from the central equatorial Pacific Ocean. *In* Mayer, L., Theyer, F., Thomas, E., et al., *Init. Repts. DSDP, 85*: Washington (U.S. Govt. Printing Office), 655–694.
- , 1990. Late Cretaceous through Neogene deep-sea benthic foraminifers (Maud Rise, Weddell Sea, Antarctica). *In* Barker, P.F., Kennett, J.P., et al., *Proc. ODP, Sci. Results, 113*: College Station, TX (Ocean Drilling Program), 571–594.
- Thomas, E., and Shackleton, N., 1996. The Palaeocene–Eocene benthic foraminiferal extinction and stable isotope anomalies. *In* Knox, R.W.O’B., Corfield, R.M., and Dunay, R.E. (Eds.), *Correlation of the Early Paleogene in Northwest Europe*. Geol. Soc. Spec. Publ., 101:401–441.
- Tiedemann, R., Sarnthein, M., and Shackleton, N.J., 1994. Astronomic timescale for the Pliocene Atlantic $\delta^{18}\text{O}$ and dust flux records of Ocean Drilling Program Site 659. *Paleoceanography, 9*:619–638.
- Tjalsma, R.C., and Lohmann, G.P., 1983. *Paleocene–Eocene Bathyal and Abyssal Benthic Foraminifera from the Atlantic Ocean*. Micropaleontology, Spec. Publ., Vol. 4.
- Torrence, C., and Compo, G.P., 1998. A practical guide to wavelet analysis. *Bull. Am. Meteorol. Soc.*, 79:61–78.
- Toumarkine, M., and Luterbacher, H., 1985. Paleocene and Eocene planktic foraminifera. *In* Bolli, H.M., Saunders, J.B., and Perch-Nielsen, K. (Eds.), *Plankton Stratigraphy*: Cambridge (Cambridge Univ. Press), 87–154.
- Van Couvering, J.A., Castradori, D., Cita, M.B., Hilgen, F.J., and Rio, D., 1998. The Global Standard Stratotype section and point (GSSP) of the Zanclean Stage and Pliocene series. *Neogene Newsl.*, 5:22–54.
- van Morkhoven, F.P.C.M., Berggren, W.A., and Edwards, A.S., 1986. *Cenozoic Cosmopolitan Deep-Water Benthic Foraminifera*. Bull. Cent. Rech. Explor.—Prod. Elf-Aquitaine, 11.
- Von Herzen, R.P., and Maxwell, A.E., 1959. The measurement of thermal conductivity of deep-sea sediments by a needle-probe method. *J. Geophys. Res.*, 64:1557–1563.
- Widmark, J.G.V., 1997. Deep-sea benthic foraminifera from Cretaceous–Tertiary boundary strata in the South Atlantic Ocean: taxonomy and paleoecology. *Fossils Strata, 43*:1–94.
- Wilson, W.D., 1960. Speed of sound in seawater as a function of temperature, pressure and salinity. *J. Acoust. Soc. Am.*, 32:641–644.
- Wyllie, M.R.J., Gregory, A.R., and Gardner, L.W., 1956. Elastic wave velocities in heterogeneous and porous media. *Geophysics, 21*:41–70.

Figure F1. Sediment classification of Leg 208. A. Ternary diagram for calcareous, siliceous, and siliclastic end-member lithologies. B. Ternary diagram for siliclastic lithologies.

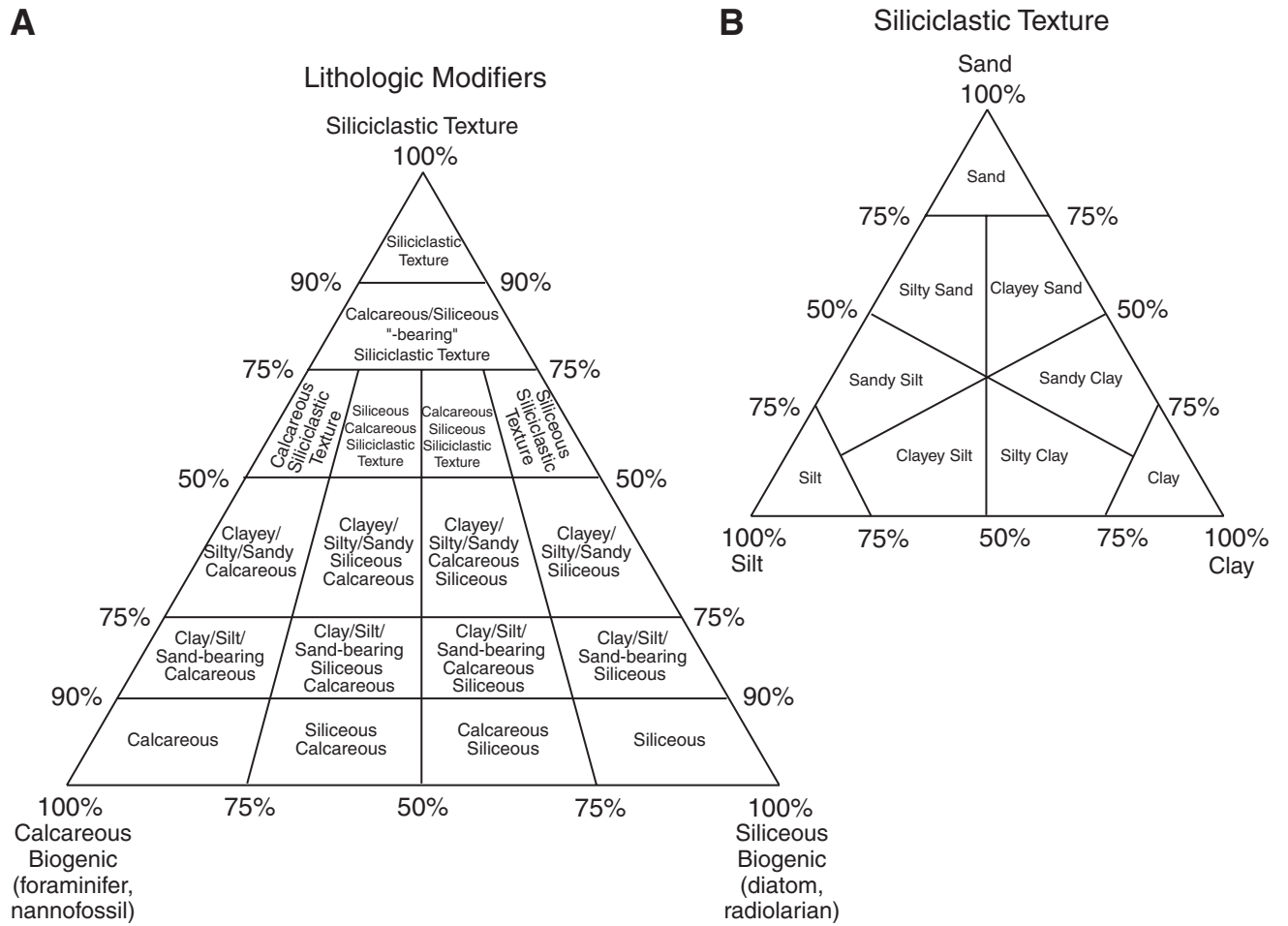


Figure F2. Comparative example of smoothed and unsmoothed core surfaces from a digital core image (interval 208-1267A-14H-1, 110–130 cm). Left half: archive-half surface smoothed as outlined in text. Right half: archive-half surface unsmoothed as produced by wire cutting.

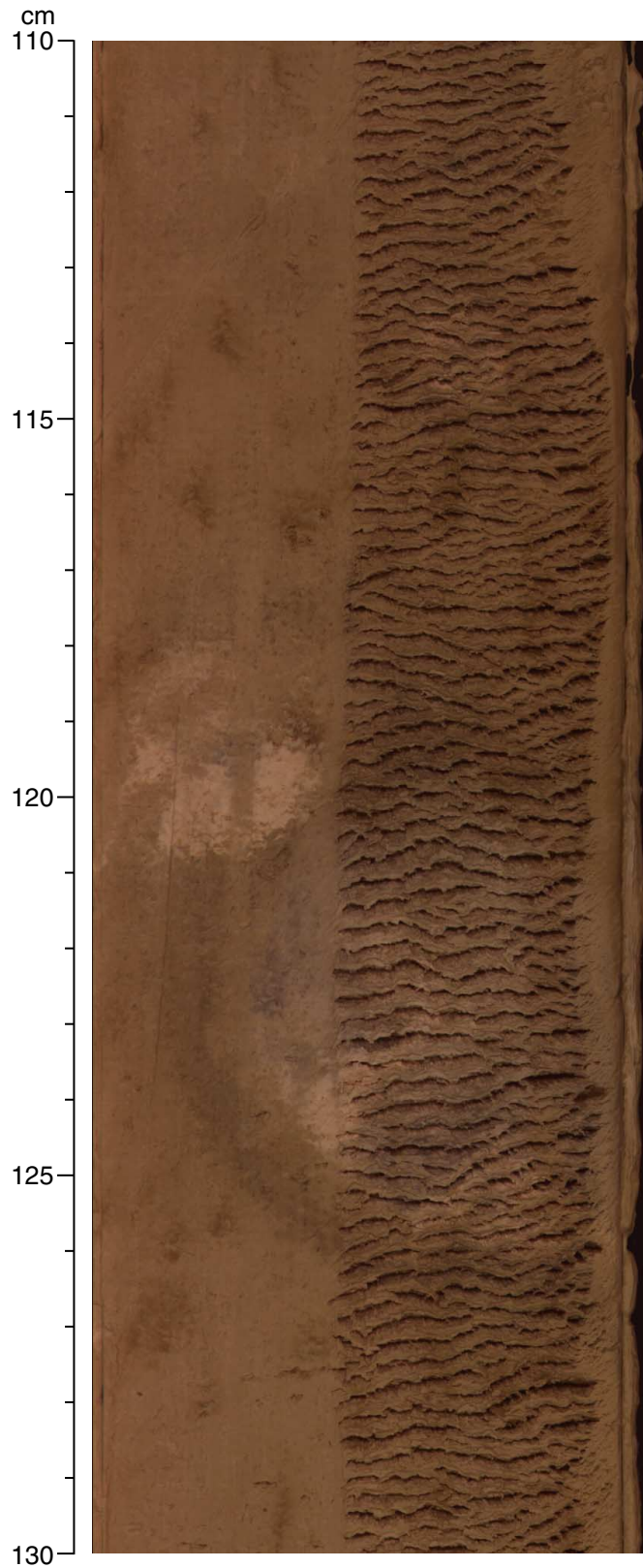


Figure F3. Key for graphic symbols used in barrel sheets.

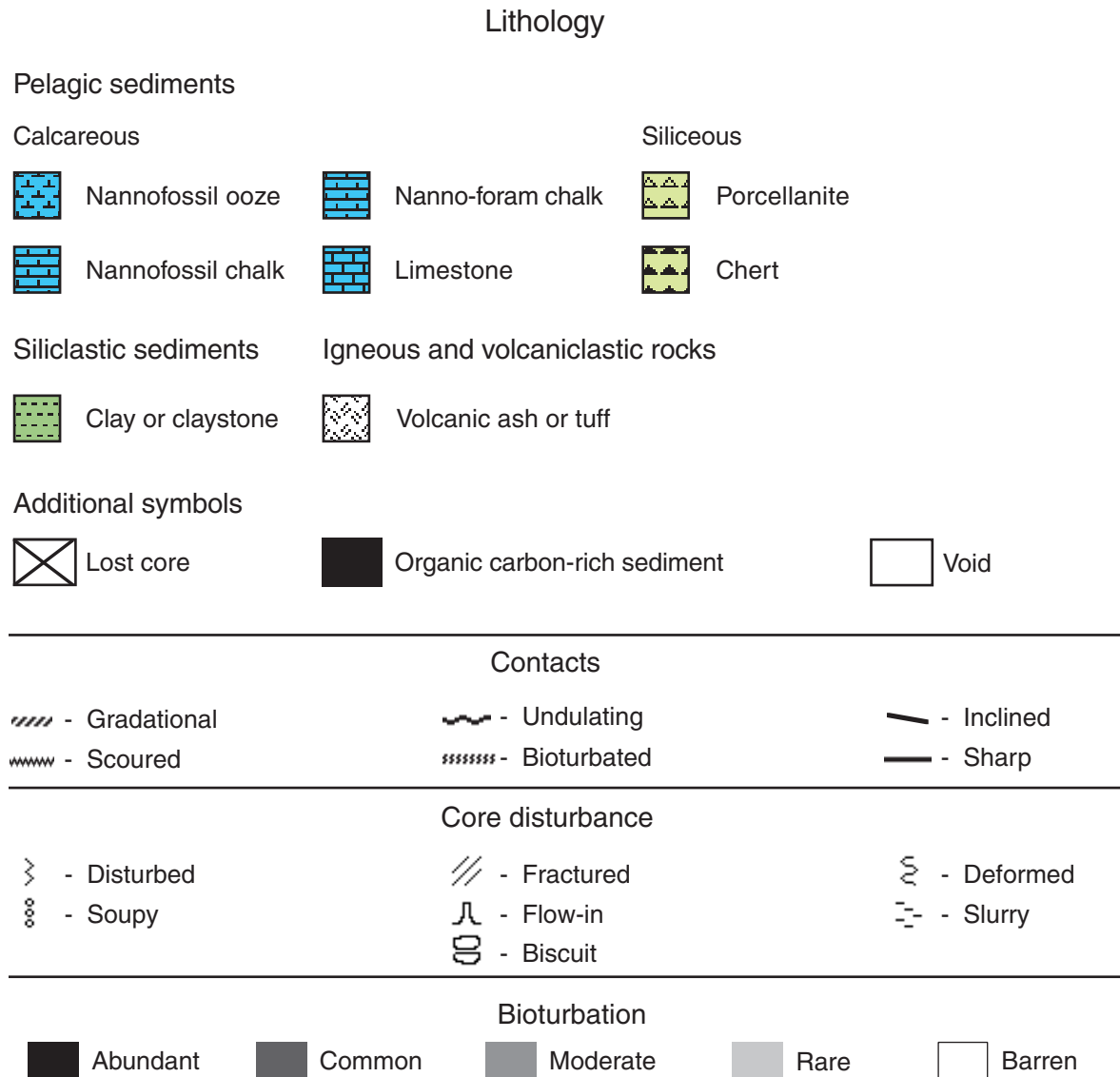


Figure F4. Calcareous nannofossil and planktonic foraminiferal zonation used during Leg 208. References are cited in the text for each microfossil group. Shaded bands with dashed lines indicate that the zonal boundaries are not clearly delimited. All information and references are given in Tables T1, p. 52, T2, p. 54, and T3, p. 57. TC = top of common occurrence, BC = bottom of common occurrence. CK95 = Cande and Kent, 1995. (Continued on next four pages.)

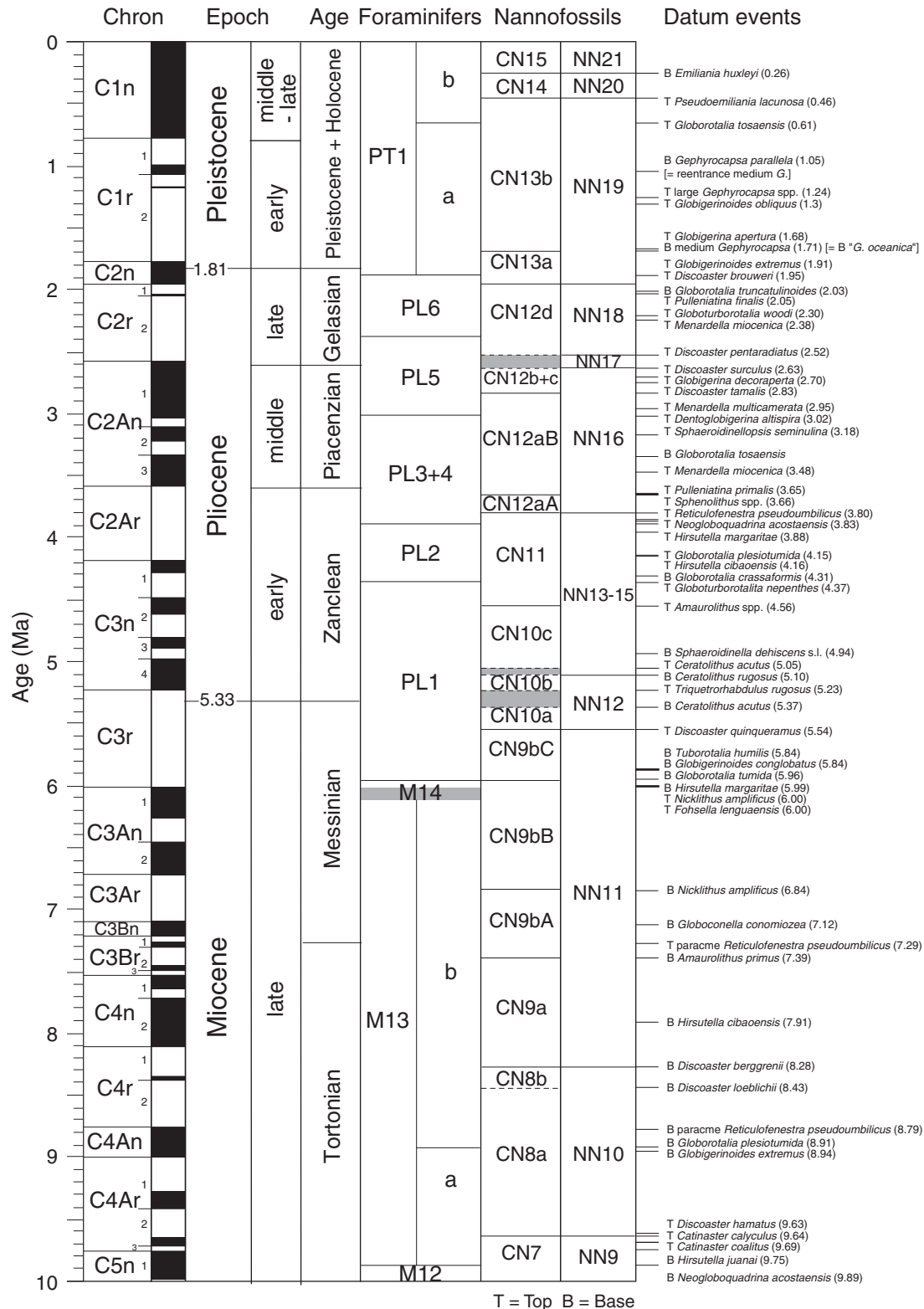


Figure F4 (continued).

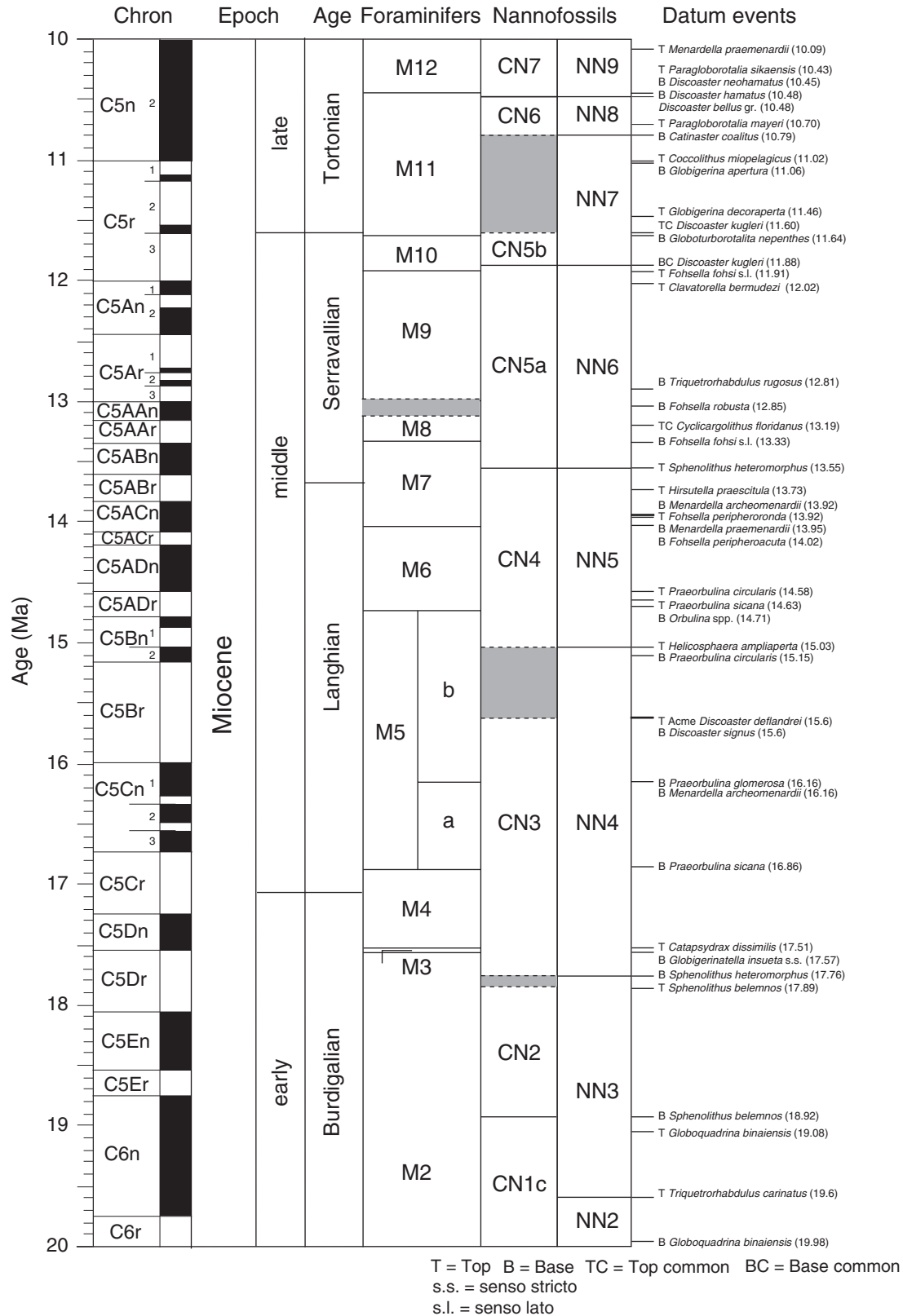


Figure F4 (continued).

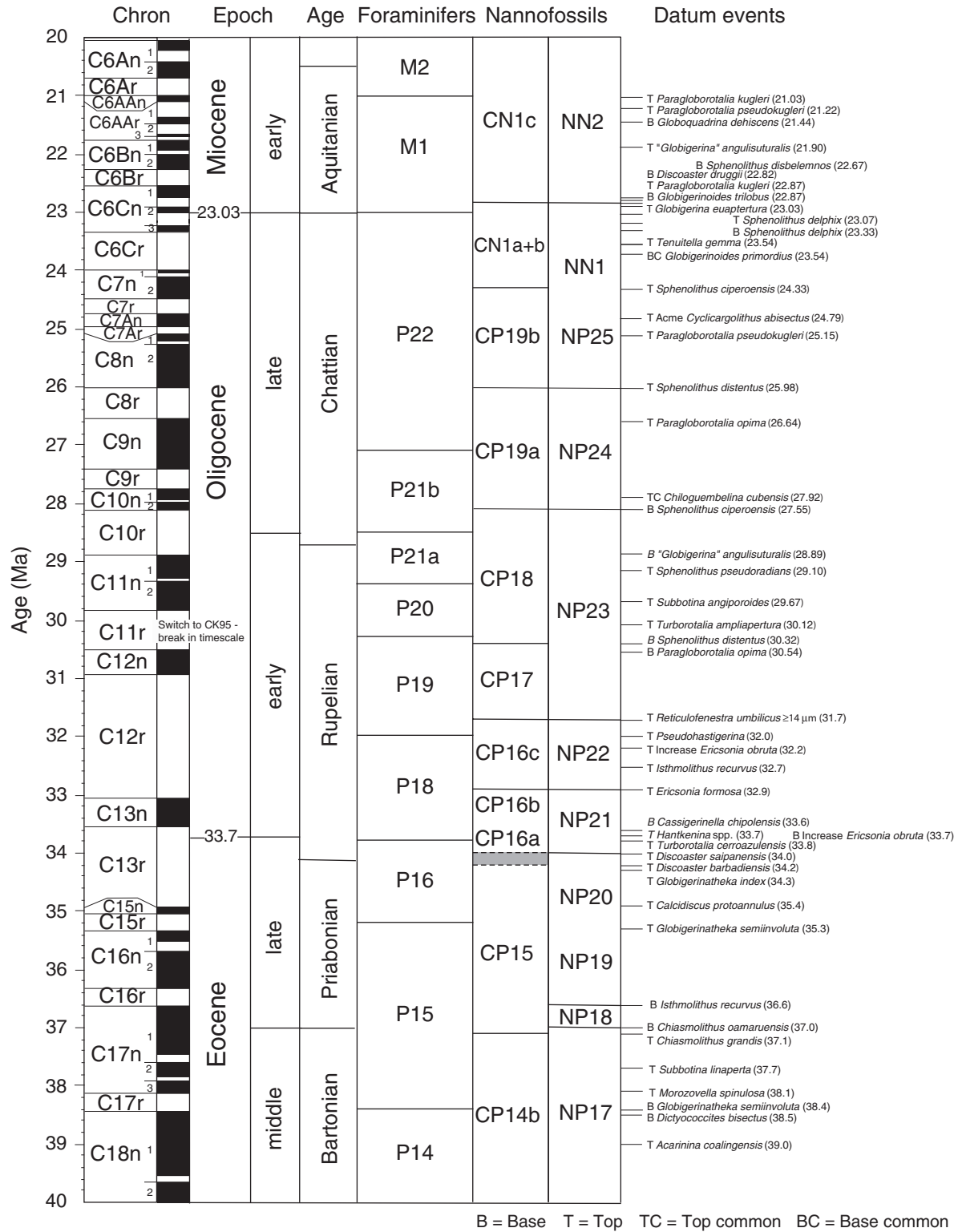


Figure F4 (continued).

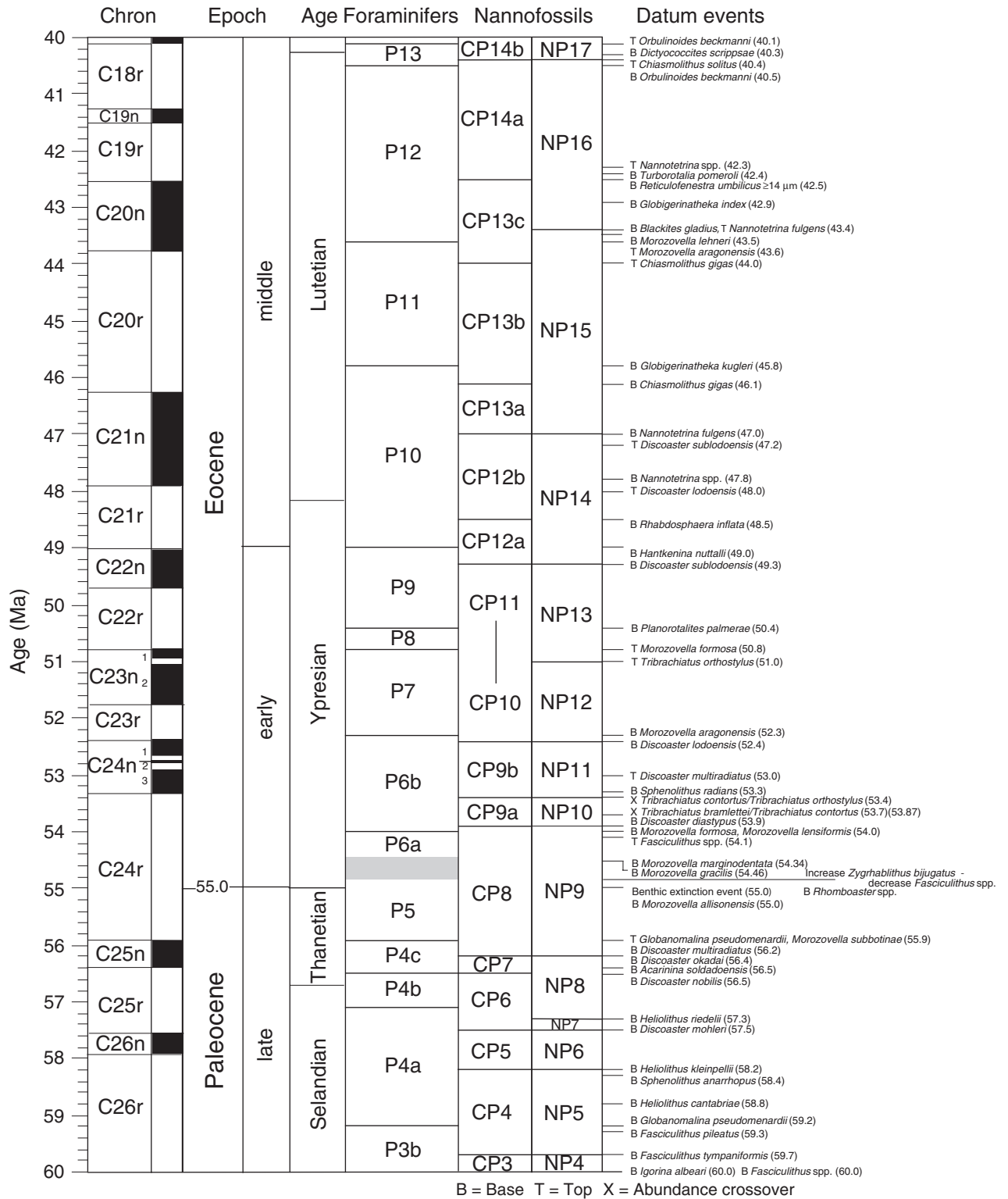


Figure F4 (continued).

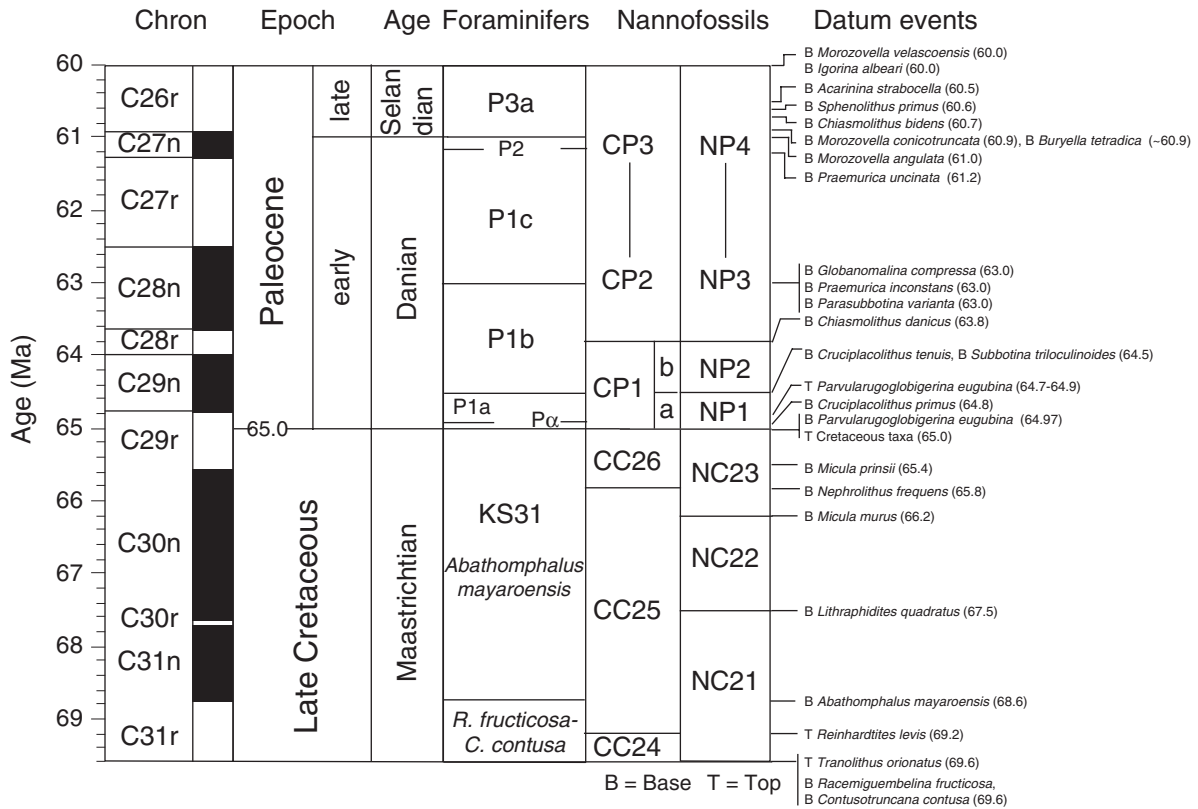


Figure F5. Example of bias in measured declination data. **A.** Declination data from unoriented archive halves from Hole 1266A. Declinations should be random but instead show a clear bias toward 0°. **B.** Declination data after core orientation with the Tensor tool (local declination = -22.73°). **C.** Declination data from unoriented whole cores from Hole 1266C. **D.** Declination data after core orientation with the Tensor tool. Declinations from the whole cores more closely approximate the expected bimodal distribution around 0° and 180°, although the distribution is far from ideal.

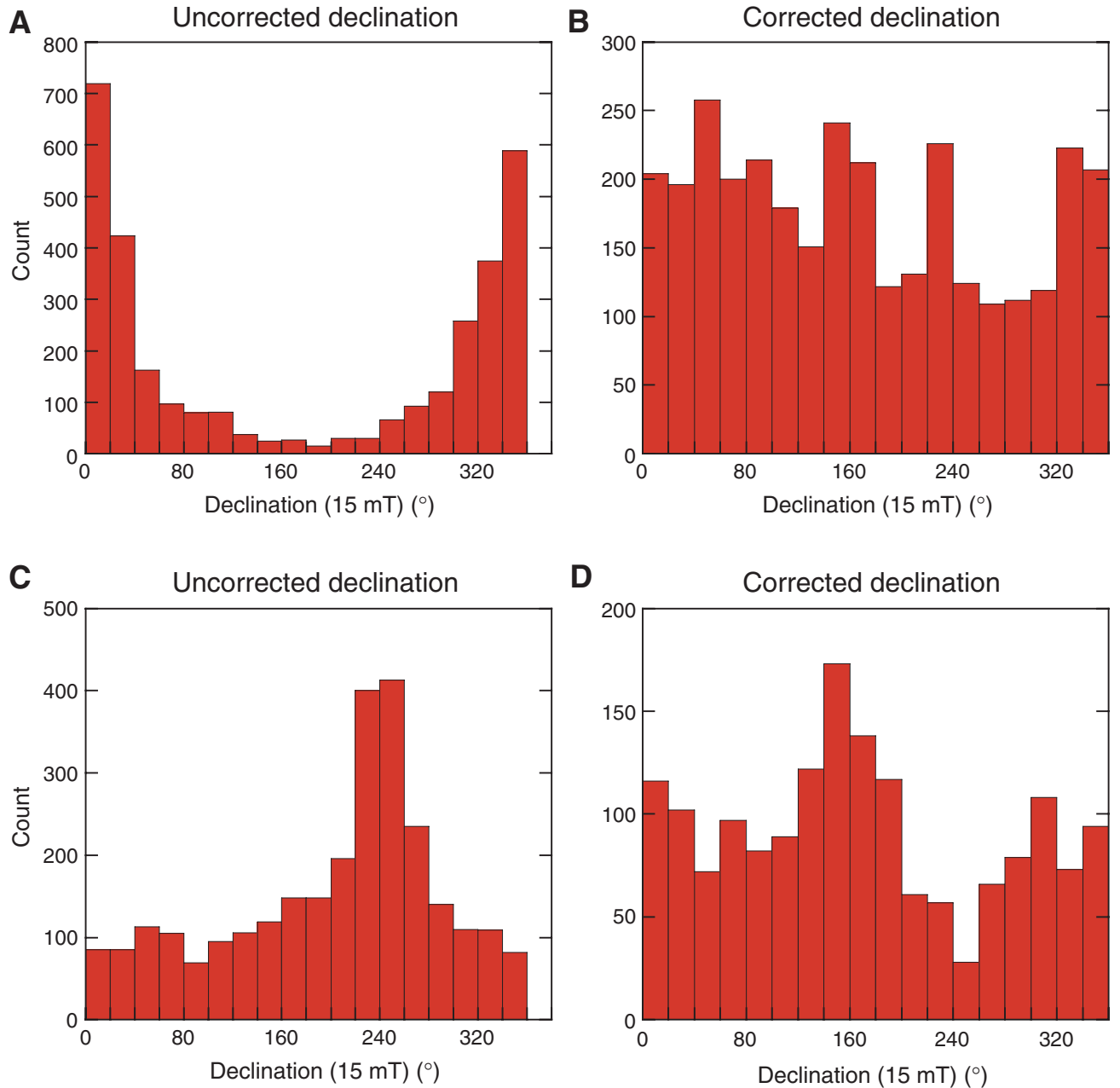


Figure F6. Schematic illustration of the configurations of tool strings used during Leg 208. See Table T8, p. 62, for explanations of the acronyms.

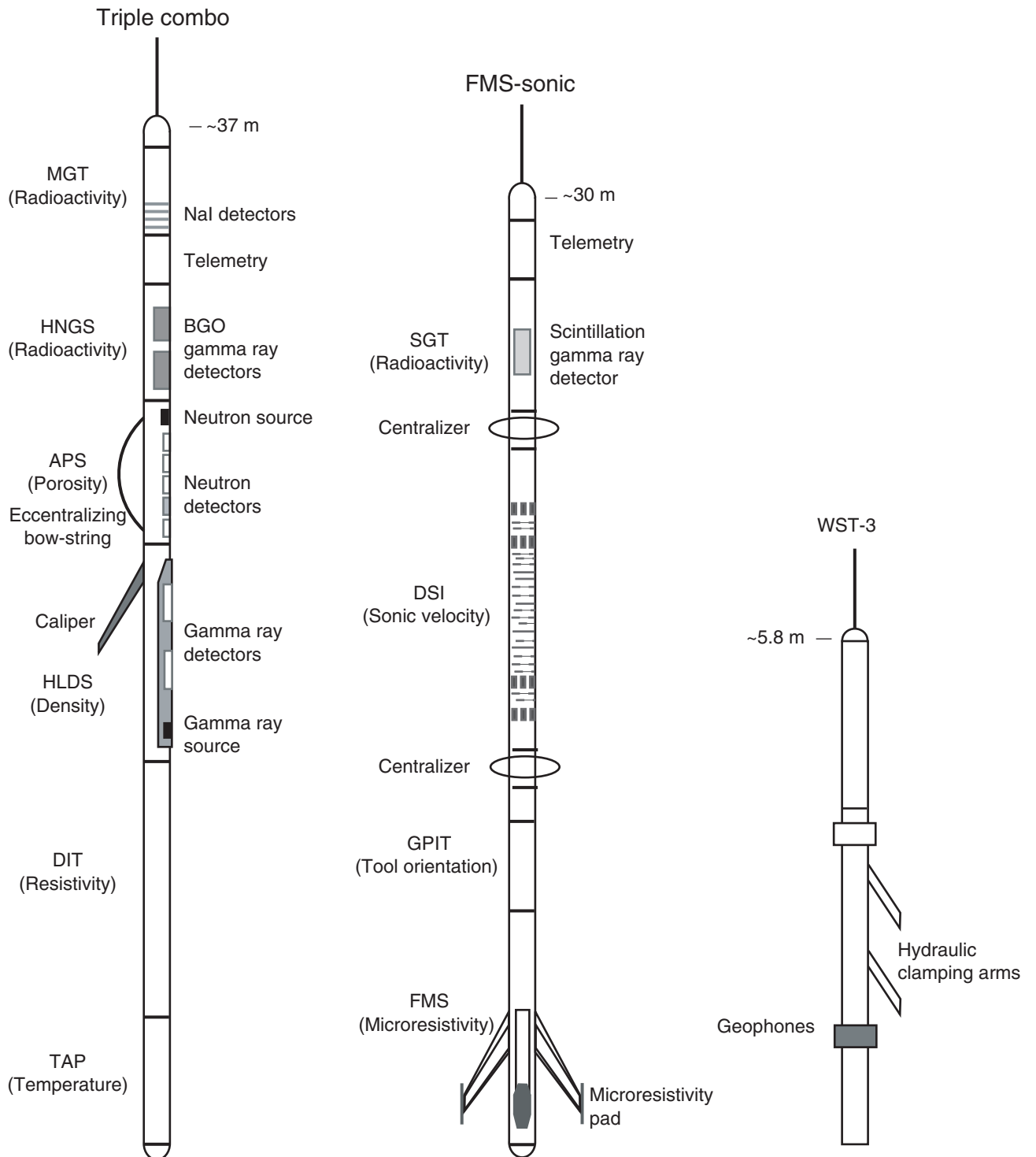


Table T1. Cenozoic and Mesozoic calcareous nannofossil datums, Leg 208. (See table notes. Continued on next page.)

	Species event	Zone/Subzone (base)	Age (Ma)	Reference	Age (Ma)	Reference
B	<i>Emiliania huxleyi</i>	CN15/NN21	0.26	1		
T	<i>Pseudoemiliania lacunosa</i>	CN14b/NN20	0.46	1		
B	<i>Gephyrocapsa parallela</i> (= reentrance medium G.)		1.01	2		
T	Large <i>Gephyrocapsa</i> spp.		1.24	2		
B	Medium <i>Gephyrocapsa</i> spp.	CN13b	1.71	2		
Pliocene/Pleistocene boundary			1.81	3		
T	<i>Discoaster brouweri</i>	CN13a/NN19	1.95	4		
T	<i>Discoaster pentaradiatus</i>	CN12d/NN18	2.52	5		
T	<i>Discoaster surculus</i>	CN12c/NN17	2.63	5		
T	<i>Discoaster tamalis</i>	CN12b+c	2.83	5		
T	<i>Sphenolithus</i> spp.	CN12aB*	3.66	6		
T	<i>Reticulofenestra pseudumbilicus</i>	CN12aA*/NN16	3.80	6		
T	<i>Amaurolithus</i> spp.	CN11	4.56	6		
T	<i>Ceratolithus acutus</i>	CN10c/NN13	5.05	7		
B	<i>Ceratolithus rugosus</i>	CN10c/NN13	5.10	7		
T	<i>Triquetrorhabdulus rugosus</i>		5.23	7		
Miocene/Pliocene boundary			5.32	8		
B	<i>Ceratolithus acutus</i>	CN10b	5.37	7		
T	<i>Discoaster quinquerramus</i>	CN10a/NN12	5.54	7		
T	<i>Nicklithus amplifucus</i>	CN9bC*	6.00	7		
B	<i>Nicklithus amplifucus</i>	CN9bB*	6.84	7		
T	Paracme <i>Reticulofenestra pseudumbilicus</i>		7.29	7		
B	<i>Amaurolithus primus</i>	CN9bA*	7.39	7		
B	<i>Discoaster berggrenii</i>	CN9a/NN11	8.28	7		
B	<i>Discoaster loeblichii</i>	CN8b	8.43	6		
B	Paracme <i>Reticulofenestra pseudumbilicus</i>		8.79	7		
T	<i>Discoaster hamatus</i>	CN8a/NN10	9.63	7		
T	<i>Catinaster calyculus</i>		9.64	7		
T	<i>Catinaster coalitus</i>		9.69	7		
B	<i>Discoaster neohamatus</i>		10.45	7		
B	<i>Discoaster hamatus</i>	CN7a/NN9	10.48	7		
B	<i>Catinaster coalitus</i>	CN6/NN8	10.79	7		
T	<i>Coccolithus miopelagicus</i>		11.02	7		
TC	<i>Discoaster kugleri</i>		11.60	7		
BC	<i>Discoaster kugleri</i>	CN5b/NN7	11.88	7		
B	<i>Triquetrorhabdulus rugosus</i>		12.81	6		
TC	<i>Cyclicargolithus floridanus</i>		13.19	6		
T	<i>Sphenolithus heteromorphus</i>	CN5a/NN6	13.55	9		
T	<i>Helicosphaera ampliaptera</i>	CN4/NN5	15.03	10		
T	Acme <i>Discoaster deflandrei</i>		15.60	10		
B	<i>Discoaster signus</i>		15.60	10		
B	<i>Sphenolithus heteromorphus</i>	CN3	17.76	11		
T	<i>Sphenolithus belemnus</i>	CN3/NN4	17.89	11		
T	<i>Triquetrorhabdulus carinatus</i>	NN3	18.36	11		
B	<i>Sphenolithus belemnus</i>	CN2	18.92	11		
B	<i>Sphenolithus disbelemnus</i>		22.76	11		
B	<i>Discoaster druggii</i>	CN1c/NN2	22.82	11		
Oligocene/Miocene boundary			23.03	11		
T	<i>Sphenolithus delphix</i>		23.07	11		
B	<i>Sphenolithus delphix</i>		23.33	12		
T	<i>Sphenolithus ciperoensis</i>	CN1a	24.23	12		
T	Acme <i>Cyclicargolithus abisectus</i>	CN1b	24.79	12		
T	<i>Sphenolithus distentus</i>	CP19b/NP25	25.98	12		
B	<i>Sphenolithus ciperoensis</i>	CP19a/NP24	27.55	12		
T	<i>Sphenolithus pseudoradians</i>		29.1	13		
B	<i>Sphenolithus distentus</i>	CP18	30.32	12		
T	<i>Reticulofenestra umbilicus</i> $\geq 14 \mu\text{m}$	CP17/NP23	31.7	14		
T	Increase <i>Ericsonia obruta</i>	CP16b	32.2	14		
T	<i>Isthmolithus recurvus</i>		32.7	14		
T	<i>Ericsonia formosa</i>	CP16c/NP22	32.9	14		
B	Increase <i>Ericsonia obruta</i>		33.7	14		
Eocene/Oligocene boundary			33.7	13		
T	<i>Discoaster saipanensis</i>	CP16a/NP21	34.0	14		
T	<i>Discoaster barbadiensis</i>	CP16a	34.2	14		
T	<i>Calcidiscus protoannulus</i>		34.9	15		
B	<i>Isthmolithus recurvus</i>	NP19	36.6	14		

Table T1 (continued).

	Species event	Zone/Subzone (base)	Age (Ma)	Reference	Age (Ma)	Reference
B	<i>Chiasmolithus oamaruensis</i>	NP18	37.0	13		
T	<i>Chiasmolithus grandis</i>	CP15	37.1	14		
B	<i>Dictyococcites bisectus</i>		38.5	16		
B	<i>Dictyococcites scrippsae</i>		40.3	14		
T	<i>Chiasmolithus solitus</i>	CP14b/NP17	40.4	13		
T	<i>Nannotetrina</i> spp.		42.3	14		
B	<i>Reticulofenestra umbilicus</i> $\geq 14 \mu\text{m}$	CP14a	42.5	14		
T	<i>Blackites gladius</i>	NP16	43.4	13		
T	<i>Nannotetrina fulgens</i>		43.4	17		
T	<i>Chiasmolithus gigas</i>	CP13c	44.0	17		
B	<i>Chiasmolithus gigas</i>	CP13b	46.1	13		
B	<i>Nannotetrina fulgens</i>	CP13a/NP15	47.0	17		
T	<i>Discoaster sublodoensis</i>		47.2	17		
B	<i>Nannotetrina</i> spp.		47.8	17		
T	<i>Discoaster lodoensis</i>		48.0	17		
B	<i>Rhabdosphaera inflata</i>	CP12b	48.5	13		
B	<i>Discoaster sublodoensis</i>	CP12a/NP14	49.3	17		
T	<i>Tribrachiatius orthostylus</i>	NP13	51.0	17		
B	<i>Toweius crassus</i>	CP11	51.5	13		
B	<i>Discoaster lodoensis</i>	CP10/NP12	52.4	17		
T	<i>Discoaster multiradiatus</i>		53.0	17		
B	<i>Sphenolithus radians</i>		53.3	17		
B	<i>Tribrachiatius orthostylus</i>	CP9b/NP11	53.4	17	53.400	18
X	<i>Tribrachiatius bramlettei/Tribrachiatius contortus</i>		53.7	17	53.875	18
B	<i>Discoaster diastypus</i>	CP9a	53.9	17		
B	<i>Tribrachiatius bramlettei</i>	CP9a/NP10	53.9	17	54.359	18
B	<i>Rhomboaster cuspis</i>		54.1	17		
T	<i>Fasciculithus</i> spp.		54.1	17		
Paleocene/Eocene boundary [†]			55.0	19		
B	<i>Discoaster multiradiatus</i>	CP8/NP9	56.2	17		
B	<i>Discoaster okadae</i>		56.4	17		
B	<i>Discoaster nobilis</i>	CP7	56.5	17		
B	<i>Heliolithus riedelii</i>	NP8	57.3	13		
B	<i>Discoaster mohleri</i>	CP6/NP7	57.5	17		
B	<i>Heliolithus kleinpellii</i>	CP5/NP6	58.2	17		
B	<i>Sphenolithus anarrhopus</i>		58.4	15		
B	<i>Heliolithus cantabriae</i>		58.8	17		
B	<i>Fasciculithus pileatus</i>		59.3	17		
B	<i>Fasciculithus tymaniformis</i>	CP4/NP5	59.7	13		
B	<i>Fasciculithus</i> spp.		60.0	17		
B	<i>Sphenolithus</i> spp.		60.7	17		
B	<i>Ellipsolithus macellus</i>	CP3/NP4	62.6	13		
B	<i>Chiasmolithus danicus</i>	CP2/NP3	64.2	13		
B	<i>Cruciplacolithus tenuis</i> s.s.	CP1b/NP2	64.5	13		
Cretaceous/Paleogene boundary			65.0			
T	Cretaceous taxa (<i>Micula prinsii</i>)		65.0	13		
B	<i>Micula prinsii</i>		65.4	20		
B	<i>Nephrolithus frequens</i>	CC26	65.8	20, 21		
B	<i>Micula murus</i>	NC23	66.2	20		
B	<i>Lithraphidites quadratus</i>	NC22	67.5	20		
T	<i>Reinhardtites levis</i>	CC25	69.2	20, 21		

Notes: B = base, T = top, TC = top common, BC = base common, X = abundance crossover. Bold = astrochronologically tuned datums. References: 1 = Thierstein et al. (1977); 2 = Raffi (2002); 3 = Lourens et al. (1996); 4 = Raffi et al. (1993); 5 = Tiedemann et al. (1994); 6 = Raffi and Flores (1995); 7 = Backman and Raffi (1997); 8 = Van Couvering et al. (1998); 9 = Shackleton et al. (1999); 10 = Shackleton et al. (2001); 11 = Lourens et al. (in press); 12 = H. Pälike et al. (pers. comm., 2003); 13 = Berggren et al. (1995b); 14 = Backman (1987); 15 = Coccioni et al. (1988); 16 = Monechi and Thierstein (1985); 17 = Backman (1986); 18 = Lyle, Wilson, Janecek, et al. (2002); 19 = Norris and Röhl (1999); 20 = Erba et al. (1995); 21 = Singh (1977). * = further subdivision of subzones (CN12aB, etc.) according to Bukry (1991) and Raffi and Flores (1995). † = carbon isotope excursion calibrated by astronomically tuning at ODP Site 1051 (Röhl et al., 2003).

Table T2. Cenozoic and Mesozoic planktonic foraminiferal datums, Leg 208. (See [table notes](#). Continued on next two pages.)

	Species event	Zone/Subzone (base)	Age (Ma)	Reference	Age (Ma)	Reference	Comment
T	<i>Globorotalia tosaensis</i>	PT1b	0.65	1	0.61	9	
T	<i>Globigerinoides obliquus</i>		1.30	3	1.30	9	
T	<i>Globigerina apertura</i>		1.64	3	1.68	9	
Pliocene/Pleistocene boundary			1.81	7	1.81	9	
T	<i>Globigerinoides extremus</i>		1.98	3	1.91	9	
B	<i>Globorotalia truncatulinoides</i>	N22	1.92	3	2.03	9	
B	<i>Pulleniatina finalis</i>		2.04	3	2.05	9	
	<i>Pulleniatina reappearance</i>		2.26	3	2.28	9	
T	<i>Globoturborotalita woodi</i>		2.33	3	2.30	9	
T	<i>Menardella miocenica</i>	PL6	2.38	3	2.38	9	
T	<i>Globigerina decoraperta</i>		2.75	3	2.70	9	
T	<i>Dentoglobigerina altispira</i>	PL5	3.11	3	3.02	9	
T	<i>Sphaeroidinellopsis seminulina</i>	PL4	3.11	3	3.18	9	
B	<i>Globorotalia tosaensis</i>	N21	3.35	1			??
	<i>Pulleniatina disappearance</i>		3.41	3	3.48	9	
B	<i>Menardella miocenica</i>		3.77	3	3.48	9	
T	<i>Hirsutella margaritae</i>	PL3	3.85	3	3.88	9	
T	<i>Neogloboquadrina acostaensis</i>				3.83	9	
T	<i>Globorotalia plesiotumida</i>		3.77	3	4.15	9	
T	<i>Hirsutella cibaensis</i>		4.60	2	4.16	9	
B	<i>Globorotalia crassaformis</i> s.l.		4.31	3	4.31	9	
T	<i>Globoturborotalita nepenthes</i>	PL2	4.39	3	4.37	9	
B	<i>Sphaeroidinella dehiscens</i> s.l.	N19	5.54	3	4.94	9	
Miocene/Pliocene boundary			5.32	9	5.33	9	
B	<i>Globigerinoides conglobatus</i>		6.20	3	5.84	9	
B	<i>Globorotalia tumida</i>	N18/PL1	5.82	3	5.96	9	
B	<i>Hirsutella margaritae</i>		6.09	3	5.99	9	
B	<i>Globocconella conomiozea</i>	Base Mt10	7.12 (6.9)	2			
B	<i>Hirsutella cibaensis</i>				7.91	9	
B	<i>Globorotalia plesiotumida</i>	N17/M13b	8.58	3	8.91	9	
B	<i>Globigerinoides extremus</i>		8.58	3	8.94	9	
B	<i>Hirsutella juanai</i>		9.76	3	9.75	9	
B	<i>Neogloboquadrina acostaensis</i>	N16/M13a	9.82	3	9.89	9	
T	<i>Paragloborotalia siakensis</i>	N15/M12			10.43	9	
T	<i>Paragloborotalia mayeri</i>	Base Mt9	10.49	3	10.70	9	
T	<i>Menardella praemenardii</i>				10.09	9	
B	<i>Globigerina apertura</i>				11.06	9	
B	<i>Hirsutella challengerii</i>				11.14	9	
B	<i>Globigerina decoraperta</i>		11.46	3	11.43	9	
B	<i>Globoturborotalita nepenthes</i>	N14/M11/Mt8	11.19	3	11.64	9	
T	<i>Clavatorella bermudezi</i>				12.02	9	
B	<i>Sphaeroidinellopsis subdehiscens</i>	N13a			13.03	9	
B	<i>Fohsella praefohsi</i>	N11/M7b			13.45	9	
B	<i>Hirsutella praescitula</i>				13.73	9	
T	<i>Menardella archaeomenardii</i>		14.20	4	13.92	9	
T	<i>Fohsella peripheroronda</i>	Base Mt7	14.20	4	13.92	9	
B	<i>Menardella praemenardii</i>		14.90	4	13.95	9	
B	<i>Fohsella periphoraocuta</i>	N10/M7a	14.70	4	14.02	9	
T	<i>Globigerinatella insueta</i>				14.50	9	
T	<i>Praeorbulina circularis</i>				14.58	9	
T	<i>Praeorbulina sicana</i>		14.80	4	14.63	9	
B	<i>Clavatorella bermudezi</i>				14.70	9	
B	<i>Orbulina suturalis</i>	Base Mt6			14.70	9	
B	<i>Orbulina</i> spp.	N9/M6	15.10	4	14.71	9	
B	<i>Praeorbulina circularis</i>		16.00	4	15.15	9	
B	<i>Menardella archaeomenardii</i>				16.16	9	
B	<i>Praeorbulina glomerosa</i>	M5b	16.10	4	16.16	9	
B	<i>Praeorbulina sicana</i>	N8/M5a	16.40	4	16.86	9	
T	<i>Catapsydrax dissimilis</i>	N7/M4a	17.30	4	17.51	9	
B	<i>Globigerinatella insueta</i> s.s.	N6/M3	18.80	4	17.57	9	
T	<i>Globoquadrina binaiensis</i>		19.10	4	19.08	9	
B	<i>Globoquadrina binaiensis</i>				19.98	9	
B	<i>Globigerinoides altiapertura</i>		20.50	2			
T	<i>Paragloborotalia kugleri</i>	N5/M2	21.50	2	21.03	9	
B	<i>Globorotalia incognita</i>		21.60	2			
T	<i>Paragloborotalia pseudokugleri</i>		21.60	2	21.22	9	
T	<i>Globigerina angulisuturalis</i>		21.60	2			

Table T2 (continued).

	Species event	Zone/Subzone (base)	Age (Ma)	Reference	Age (Ma)	Reference	Comment
B	<i>Globoquadrina dehiscens</i>		23.20	2	21.44	9	
B	<i>Globigerinoides trilobus</i> s.l.		23.40	4	22.87	9	
B	<i>Paragloborotalia kugleri</i>	N4/M1	23.80	2	22.87	9	
Oligocene/Miocene boundary			23.80	2	23.03		
T	<i>Globigerina euapertura</i>		23.80	2	23.03		
T	<i>Tenuitella gemma</i>		24.30	2	23.54		
B	<i>Globigerinoides primordius</i> (common)		24.30	2	23.54		
B	<i>Paragloborotalia pseudokugleri</i>		25.90	2	25.15		
B	<i>Globigerinoides primordius</i>		26.70	2	26.22		
T	<i>Globigerina labiacrassata</i>		27.10	2	26.64		
T	<i>Paragloborotalia opima</i>	P22	27.10	2	26.64		
T	<i>Chiloguembelina cubensis</i> (common)	P21b	28.50	2	27.92		
B	<i>Globigerina angulisuturalis</i>	P21a	29.40	2	28.89		
T	<i>Subbotina angiporoides</i>		30.00	2	29.67		
T	<i>Turborotalia ampliapertura</i>	P20	30.30	2	30.12		
B	<i>Paragloborotalia opima</i>		30.60	2	30.54		
T	<i>Pseudohastigerina</i> spp.	P19	32.00	2			
B	<i>Cassigerinella chipolensis</i>		33.65	2			
Eocene/Oligocene boundary			33.70	2			
T	<i>Hantkenina</i> spp.		33.70	2			
T	<i>Turborotalia cerroazulensis</i>	P18	33.80	2			
T	<i>Cribohantkenina inflata</i>	P17	34.00	2			
T	<i>Globigerinatheka index</i>		34.30	2			
B	<i>Turborotalia cunialensis</i>	P16	35.20	2			
T	<i>Turborotalia pomeroli</i>		35.30	2			
T	<i>Globigerinatheka semiinvoluta</i>		35.30	2			
B	<i>Cribohantkenina inflata</i>		35.50	2			
T	<i>Acarinina collactea</i>		37.70	2			
T	<i>Subbotina linaperta</i>		37.70	2			
T	<i>Morozovella spinulosa</i>		38.10	2			
B	<i>Globigerinatheka semiinvoluta</i>	P15	38.40	2			
T	<i>Planorotalites</i> spp.		38.50	2			
T	<i>Acarinina primitiva</i>		39.00	2			
T	<i>Subbotina frontosa</i>		39.30	2			
T	<i>Orbulinoides beckmanni</i>	P14	40.10	2			
B	<i>Orbulinoides beckmanni</i>	P13	40.50	2			
T	<i>Acarinina bullbrooki</i>		40.50	2			
B	<i>Turborotalia pomeroli</i>		42.40	2			
B	<i>Globigerinatheka index</i>		42.90	2			
B	<i>Morozovella lehneri</i>		43.50	2			
T	<i>Morozovella aragonensis</i>	P12	43.60	2			
B	<i>Globigerinatheka kugleri</i>	P11	45.80	2			
B	<i>Turborotalia possagnoensis</i>		46.00	2			
B	<i>Hantkenina nuttalli</i>	P10	49.00	2			
B	<i>Planorotalites palmerae</i>	P9	50.40	2			
T	<i>Morozovella formosa</i>	P8	50.80	2			
B	<i>Acarinina pentacamerata</i>		50.80	2			
B	<i>Morozovella aragonensis</i>	P7	52.30	2	52.76	6	
T	<i>Morozovella marginodentata</i>		52.50	2			
T	<i>Morozovella lensiformis</i>		52.70	2			
B	<i>Acarinina angulosa</i>				52.78	6	
T	<i>Subbotina velascoensis</i>		53.50	2			
B	<i>Acarinina quetra</i>				53.52	6	
T	<i>Morozovella aequa</i>		53.60	2	52.89	6	
B	<i>Morozovella formosa</i>	P6b	54.00	2			
T	<i>Subbotina triangularis</i>				54.07	6	
B	<i>Morozovella lensiformis</i>		54.00	2	53.68	6	
T	<i>Subbotina velascoensis</i>				54.17	6	
T	<i>Morozovella velascoensis</i>	P6a	54.70	2	54.31	6	
T	<i>Morozovella acuta</i>		54.70	2			
B	<i>Morozovella gracilis</i>		54.70	2	54.46	6	
B	<i>Igorina broedermanni</i>		54.70	2			
B	<i>Morozovella marginodentata</i>		54.80	2	54.34	6	
B	<i>Chiloguembelina wilcoxensis</i>				54.94	6	
B	<i>Pseudohastigerina wilcoxensis</i>				54.94	6	
Paleocene/Eocene boundary			55.00	6			
B	<i>Globanomalina australiformis</i>		55.50	2			
B	<i>Morozovella subbotinae</i>		55.90	2			

Table T2 (continued).

	Species event	Zone/Subzone (base)	Age (Ma)	Reference	Age (Ma)	Reference	Comment
T	<i>Globanomalina pseudomenardii</i>	P5	55.90	2			
T	<i>Acarinina nitida</i> (= <i>Acarinina acarinata</i>)		56.30	2			
T	<i>Acarinina mckannai</i>		56.30	2			
B	<i>Acarinina soldadoensis</i>	P4c	56.50	2			
B	<i>Acarinina coalingensis</i> (= <i>triplex</i>)		56.50	2			
B	<i>Morozovella aequa</i>		56.50	2			
B	<i>Acarinina mckannai</i>		59.10	2			
B	<i>Acarinina subsphaerica</i>		59.20	2			
B	<i>Acarinina nitida</i>		59.20	2			
B	<i>Globanomalina pseudomenardii</i>	P4a	59.20	2			
T	<i>Parasubbotina variospira</i> (= <i>variata</i> ?)		59.20	2			
T	<i>Parasubbotina variata</i>		59.20	2, 6			
B	<i>Morozovella velascoensis</i>		60.00	2			
B	<i>Igorina albeari</i>	P3b	60.00	2			
B	<i>Acarinina strabocella</i>		60.50	6			
B	<i>Morozovella conicotruncata</i>		60.90	2			
B	<i>Morozovella angulata</i>	P3a	61.00	2			
B	<i>Igorina pusilla</i>		61.00	2			
B	<i>Praemurica praeangulata</i>		61.20	2			
B	<i>Praemurica uncinata</i>	P2	61.20	2			
B	<i>Globanomalina imitata</i>		61.30	2			
B	<i>Globanomalina compressa</i>	P1c	63.00	2			
B	<i>Praemurica inconstans</i>		63.00	2			
B	<i>Parasubbotina variata</i>		63.00	2			
B	<i>Subbotina triloculinoidea</i>	P1b	64.50	2			
T	<i>Parvularugoglobigerina extensa</i>		64.90	6			
T	<i>Parvularugoglobigerina eugubina</i>	P1a	64.90	2			
B	<i>Parvularugoglobigerina eugubina</i>	Pa	64.97	2			
Maastrichtian							
T	<i>Abathomphalus mayaroensis</i>		65	2			
B	<i>Abathomphalus mayaroensis</i> (KS31)		68.6	10			
B	<i>Racemiguembelina fructicosa</i> – <i>Contusotruncana contusa</i>		69.6	10			

Notes: T = top (highest occurrence), B = bottom (lowest occurrence). Bold = astronomically tuned ages (Lourens et al., in press; H. Pälike pers. comm., 2003). References: 1 = Berggren et al. (1995a); 2 = Berggren et al. (1995b); 3 = Chaisson and Pearson (1997); 4 = Pearson and Chaisson (1997); 5 = Olsson et al. (1999); 6 = Norris and Röhl (1999); 7 = Lourens et al. (1996); 8 = Hilgen et al. (1991); 9 = Lourens et al. (in press); 10 = Premoli Silva and Sliter (1999). ?? = age not astronomically tuned.

Table T3. Benthic foraminifer depth zonation, Leg 208.

Depth		
Zone	Subzone	Range (m)
Neritic		0–200
Bathyal	Upper	200–600
	Middle	600–1000
	Lower	1000–2000
Abyssal	Upper	2000–3000
	Lower	>3000

Note: After van Morkhoven et al. (1986).

Table T4. Demagnetization of working halves and core sections, Leg 208.

Hole core, section	Maximum demagnetization (mT)
208-	
1262B-3H-1	15
1263B-29X-4	15
1264A-24H-4	15
1265B-10H-2	15
1266C-1H	10
1266C-2H	10
1266C-3H	10
1266C-4H	15
1266C-5H	15
1266C-6H	15
1266C-7H	15
1266C-8H	15
1266C-9H	15
1266C-10H	15
1266C-11H	15
1266C-12H	15
1266C-13H	15
1266C-14H	15
1266C-15H	15
1266C-16H	15
1266C-17H	15
1266C-18H	15
1266C-19X	15
1266C-20X	15
1266C-21X	15

Note: Where no section is specified, the entire core was demagnetized to the given level.

Table T5. Timescale used for magnetostratigraphic age assignments, Leg 208.

Chron	Age (Ma)				Chron	Age (Ma)			
	1		2			1		2	
	y	o	y	o		y	o	y	o
C1n	0.000	0.781	0.000	0.780	C6Bn.2n	21.992	22.268	22.804	23.069
C1r.1n	0.988	1.072	0.990	1.070	C6Cn.1n	22.564	22.754	23.353	23.535
C1r.2n	1.173	1.185	1.201	1.211	C6Cn.2n	22.902	23.030	23.677	23.800
C2n	1.785	1.942	1.770	1.950	C6Cn.3n	23.230	23.340	23.999	24.118
C2r.1n	2.129	2.149	2.140	2.150	C7n.1n	24.011	24.040	24.730	24.781
C2An.1n	2.582	3.032	2.581	3.040	C7n.2n	24.121	24.451	24.835	25.183
C2An.2n	3.116	3.207	3.110	3.220	C7An	24.781	24.942	25.496	25.648
C2An.3n	3.330	3.596	3.330	3.580	C8n.1n	25.053	25.216	25.823	25.951
C3n.1n	4.188	4.300	4.180	4.290	C8n.2n	25.250	26.061	25.992	26.554
C3n.2n	4.493	4.632	4.480	4.620	C9n	26.581	27.402	27.027	27.972
C3n.3n	4.799	4.896	4.800	4.890	C10n.1n	27.760	27.926	28.283	28.512
C3n.4n	4.998	5.236	4.980	5.230	C10n.2n	27.965	28.053	28.578	28.745
C3An.1n	6.040	6.260	5.894	6.137	C11n.1n	28.889	29.305	29.401	29.662
C3An.2n	6.440	6.710	6.269	6.567	C11n.2n	29.354	29.828	29.765	30.098
C3Bn	7.101	7.210	6.935	7.091	C12n			30.479	30.939
C3Br.1n	7.256	7.301	7.135	7.170	C13n			33.058	33.545
C3Br.2n	7.455	7.492	7.341	7.375	C15n			34.655	34.940
C4n.1n	7.532	7.644	7.432	7.562	C16n.1n			35.343	35.526
C4n.2n	7.697	8.109	7.650	8.072	C16n.2n			35.685	36.341
C4r.1n	8.256	8.302	8.225	8.257	C17n.1n			36.618	37.473
C4An	8.777	9.059	8.699	9.025	C17n.2n			37.604	37.848
C4Ar.1n	9.274	9.404	9.230	9.308	C17n.3n			37.920	38.113
C4Ar.2n	9.666	9.724	9.580	9.642	C18n.1n			38.426	39.552
C5n.1n	9.767	9.868	9.740	9.880	C18n.2n			39.631	40.130
C5n.2n	10.001	11.043	9.920	10.949	C19n			41.257	41.521
C5r.1n	11.122	11.158	11.052	11.099	C20n			42.536	43.789
C5r.2n	11.558	11.618	11.476	11.531	C21n			46.264	47.906
C5An.1n	12.018	12.118	11.935	12.078	C22n			49.037	49.714
C5An.2n	12.214	12.447	12.184	12.401	C23n.1n			50.778	50.946
C5Ar.1n	12.735	12.770	12.678	12.708	C23n.2n			51.047	51.743
C5Ar.2n	12.825	12.881	12.775	12.819	C24n.1n			52.364	52.663
C5AAn	13.015	13.183	12.991	13.139	C24n.2n			52.757	52.801
C5ABn	13.369	13.605	13.302	13.510	C24n.3n			52.903	53.347
C5ACn	13.734	14.095	13.703	14.076	C25n			55.904	56.391
C5ADn	14.194	14.581	14.178	14.612	C26n			57.554	57.911
C5Bn.1n	14.784	14.877	14.800	14.888	C27n			60.920	61.276
C5Bn.2n	15.032	15.160	15.034	15.155	C28n			62.499	63.634
C5Cn.1n	15.974	16.268	16.014	16.293	C29n			63.976	64.745
C5Cn.2n	16.303	16.472	16.327	16.488	C30n			65.578	67.610
C5Cn.3n	16.543	16.721	16.556	16.726	C31n			67.735	68.737
C5Dn	17.235	17.533	17.277	17.615	C32n.1n			71.071	71.338
C5En	18.056	18.524	18.281	18.781	C32n.2n			71.587	73.004
C6n	18.748	19.722	19.048	20.131	C32r.1n			73.291	73.374
C6An.1n	20.040	20.213	20.518	20.725	C33n			73.619	79.075
C6An.2n	20.439	20.709	20.996	21.320	C34n			83.000	118.000
C6AAn	21.083	21.159	21.768	21.859					
C6AAr.1n	21.403	21.483	22.151	22.248					
C6AAr.2n	21.659	21.688	22.459	22.493					
C6Bn.1n	21.767	21.936	22.588	22.750					

Notes: o = old end of chron, y = young end of chron. 1 = ages as in Lourens et al. (in press), 2 = ages as in Cande and Kent (1995).

Table T6. Measured parameters, analytical methods, and reproducibility ($\pm 1 \sigma$ standard deviation) of interstitial water geochemistry results, Leg 208.

Parameter	Method	Reproducibility (%)	Consistency standard (%)
Alkalinity	Gran titration	± 1.5	
pH	Gran titration	NA	
Salinity	Refractometer	NA	
Cl ⁻	Titration with AgCl	± 0.1	
SO ₄ ²⁻	Ion chromatography	± 0.1	
Li ⁺	ICP-AES	± 1.24	± 5.63
H ₃ BO ₃	ICP-AES	± 1.70	± 1.38
Na ⁺	ICP-AES	± 1.29	± 1.50
Mg ²⁺	ICP-AES	± 1.21	± 0.95
Si(OH) ₄	ICP-AES	± 2.31	± 6.72
K ⁺	ICP-AES	± 1.33	± 2.08
Ca ²⁺	ICP-AES	± 1.39	± 1.85
Mn ²⁺	ICP-AES	± 1.83	± 14.3
Fe ²⁺	ICP-AES	± 6.85	± 27.5
Zn ²⁺	ICP-AES	± 5.95	ND
Sr ²⁺	ICP-AES	± 1.51	± 3.27
Ba ²⁺	ICP-AES	± 1.46	± 7.01

Notes: NA = not applicable, ND = not determined. ICP-AES = inductively coupled plasma-atomic emission spectroscopy.

Table T7. Reproducibility ($\pm 1 \sigma$ standard deviation) of sediment dissolution ICP-AES analyses results, Leg 208.

Species	Reproducibility (%)	Consistency standard (%)
H ₃ BO ₃	± 2.41	± 9.47
Na ⁺	± 3.31	± 21.9
Mg ²⁺	± 1.15	± 5.16
K ⁺	± 2.20	± 20.9
Ca ²⁺	± 1.83	± 1.76
Mn ²⁺	± 1.22	± 2.82
Fe ²⁺	± 8.42	± 16.5
Sr ²⁺	± 0.99	± 2.97
Ba ²⁺	± 3.51	± 3.91

Note: ICP-AES = inductively coupled plasma-atomic emission spectroscopy.

Table T8. Measurements made by the wireline tool strings, Leg 208.

Tool string	Tool	Measurement	Sampling interval (cm)	Approximate vertical resolution (cm)	
Triple combination	HNGS	Spectral gamma ray	15	51	
	APS	Porosity	5 and 15	43	
	HLDS	Bulk density	2.5 and 15	38	
	DIT	Resistivity	15	76, 150, 200	
	TAP	Temperature		1 per s	NA
		Tool acceleration		4 per s	NA
		Pressure		1 per s	NA
Formation MicroScanner (FMS)	MGT	Gamma ray	15	15	
	FMS	Microresistivity	0.25	0.5	
FMS-sonic combination	GPIT	Tool orientation	0.25 and 15	NA	
	SGT	Total gamma ray	15	NA	
	DSI	Acoustic velocity	15	107	
WST (stationary measurement)	WST-3*	Sonic traveltime	Variable	NA	

Notes: All tool and tool string names (except the TAP and MGT) are trademarks of Schlumberger. For the complete list of acronyms used in the ODP and for additional information about tool physics and use consult ODP Logging Services at www.ldeo.columbia.edu/BRG/ODP. See Table T9, p. 63, for explanations of acronyms used to describe tool strings and tools. * = not included on every run. NA = not applicable.

Table T9. Acronyms and units used for wireline logging tools, Leg 208.

Tool	Output	Tool name/explanation of output	Unit
APS		Accelerator Porosity Sonde	
	APLC	Near array porosity (limestone calibrated)	%
	SIGF	Formation capture cross section (Σf)	Capture units
	STOF	Tool standoff (computed distance from borehole wall)	in
DIT		Dual Induction Tool	
	IDPH	Deep induction resistivity	Ωm
	IMPH	Medium induction resistivity	Ωm
	SFLU	Spherically focused resistivity	Ωm
DSI		Dipole Sonic Imager	
	DTCO	Compressional wave delay time (Δt)	ms/ft
	DTSM	Shear wave delay time (Δt)	ms/ft
	DTST	Stoneley wave delay time (Δt)	ms/ft
FMS		Formation MicroScanner	
	C1, C2	Orthogonal hole diameters	in
	P1AZ	Pad 1 azimuth	Degrees
		Spatially oriented resistivity images of borehole wall	
GPIT		General Purpose Inclinator Tool	
	DEVI	Hole deviation	Degrees
	HAZI	Hole azimuth	Degrees
	F_x, F_y, F_z	Earth's magnetic field (three orthogonal components)	Degrees
	A_x, A_y, A_z	Acceleration (three orthogonal components)	m/s^2
HLDS		Hostile Environment Litho-Density Sonde	
	RHOM	Bulk density	g/cm^3
	PEF	Photoelectric effect	b/e ⁻
	LCAL	Caliper (measure of borehole diameter)	in
	DRH	Bulk density correction	g/cm^3
HNGS		Hostile Environment Gamma Ray Sonde	
	HSGR	Standard (total) gamma ray	gAPI
	HCGR	Computed gamma ray (HSGR minus uranium contribution)	gAPI
	HFK	Potassium	wt%
	HTHO	Thorium	ppm
	HURA	Uranium	ppm
	HBHK	Borehole potassium	dec. fract.
MGT		Multi-Sensor Spectral Gamma Ray Tool	
	GR	Total gamma ray	gAPI
	POTA	Potassium	wt%
	THOR	Thorium	ppm
	URAN	Uranium	ppm
SGT		Scintillation Gamma Ray Tool	
	ECGR	Environmentally corrected gamma ray	gAPI
TAP		Temperature/Acceleration/Pressure tool	$^{\circ}C, m/s^2, psi$
WST-3*		Well Seismic Tool (3 components) Acoustic arrival times	ms

Notes: All tool and tool string names (except the TAP and MGT) are trademarks of Schlumberger. For the complete list of acronyms used in the ODP and for additional information about tool physics and use consult ODP Logging Services at www.ideo.columbia.edu/BRG/ODP. * = not included on every operation.